OPEN ACCESS
IOP Publishing | Songshan Lake Materials Laboratory Materials Futures
Mater. Futures 1 (2022) 012301 (24pp) https://doi.org/10.1088/2752-5724/ac49e3

Topical Review

Interface and surface engineering of black phosphorus: a review for optoelectronic and photonic applications

Haoran Mu*, Wenzhi Yu, Jian Yuan, Shenghuang Lin* and Guangyu Zhang*

Songshan Lake Materials Laboratory, Dongguan, Guangdong 523808, People's Republic of China

E-mail: muhaoran@sslab.org.cn, linshenghuang@sslab.org.cn and gyzhang@sslab.org.cn

Received 13 October 2021, revised 5 January 2022
Accepted for publication 5 January 2022
Published 31 March 2022

Abstract

Since being rediscovered as an emerging 2D material, black phosphorus (BP), with an extraordinary energy structure and unusually strong interlayer interactions, offers new opportunities for optoelectronics and photonics. However, due to the thin atomic body and the ease of degradation with water and oxides, BP is highly sensitive to the surrounding environment. Therefore, high-quality engineering of interfaces and surfaces plays an essential role in BP-based applications. In this review, begun with a review of properties of BP, different strategies of interface and surfaces engineering for high ON-OFF ratio, enhanced optical absorption, and fast optical response are reviewed and highlighted, and recent state-of-the-art advances on optoelectronic and photonic devices are demonstrated. Finally, the opportunities and challenges for future BP-related research are considered.

Keywords: black phosphorus, interface engineering, surface engineering, optoelectronics, photonics

(Some figures may appear in colour only in the online journal)

* Authors to whom any correspondence should be addressed.

Future perspectives
Owing to its atomic body thickness and free dangling bonds, black phosphorus (BP) as a typical 2D semiconductor is naturally sensitive to its interface and surface properties. Based on a comprehensive understanding of the interface of BP with semiconductor, metal, and dielectric materials, BP shows reduced contact resistance, enhanced light-matter interactions, and a variety of other novel properties. Furthermore, the two main shortcomings of BP, including the poor air stability and relatively low electron mobility, can be effectively optimized through these strategies, such as surface modification or passivation. Overall, interface and surface engineering will promote BP for next-generation optoelectronics and photonics and inspire the field of other 2D materials.

1. Introduction

As the most stable allotrope of phosphorus, black phosphorus (BP) was successfully synthesized over a hundred years ago [1]. With the emergence of two-dimensional (2D) materials such as graphene [2–5] and transition metal dichalcogenides (TMDs) [6–9], BP as an anisotropic 2D material was rediscovered in 2014 [10], attracting significant attention for future optoelectronics and photonics [11–13]. Due to the strong interlayer interaction, BP exhibits a widely tunable bandgap from 0.3 to 2.0 eV with the thickness varying from bulk to monolayer [14–17]. The moderate bandgap provides BP with the opportunity to bridge the gap between graphene with zero-gap and TMDs with relatively large bandgap and cover the near- and mid-infrared wavelength range [15, 18–20]. Furthermore, unlike TMDs, the bandgap is still direct regardless of the thickness, making BP with ultrafast carrier transitions and the thickness-dependent exciton absorption [16, 20–25]. For electronic applications, the finite and direct bandgap ensures a high charge carrier mobility, high on-off ratio, and low dark current for a transistor [10, 14, 26–29]. For optical devices, the strong interactions between BP with mid-infrared and higher energy photons result in broad bandwidth and fast photo-response [17, 26, 30–33]. Another distinct feature of BP is the in-plane anisotropy [15, 16, 22, 34–36]. Originating from the orthorhombic puckered arrangement of P atoms, BP has reduced symmetry in the momentum space, which leads to strong in-plane anisotropy in electronic, optical, and mechanical properties along armchair (AC, perpendicular to the pucker) and zigzag (*ZZ*, along the pucker) directions. The linear dichroic properties make the possibility for polarized devices. Owing to the promising properties and the ease of integration with other materials and structures, BP as the functional material has achieved wide applications, such as photodetectors [26, 30, 32, 37–39], photovoltaic devices [40–44], light-emitting diodes (LEDs) [45–47], ultrafast lasers [48–50], optical switches [51, 52], and so on.

For the fabrication of these devices, interface and surface engineering play a vital role [53–55]. Due to its atomic thickness nature like other 2D materials, few-layer BP is essentially an 'interface type' material, in which both the properties of BP and the performance of BP-based devices are susceptible to the interface and surface [56, 57]. First, intrinsic BP is a p-type semiconductor with an unbalanced hole-dominated transport behavior [14, 29]. By interface engineering or surface functionalization, the dominant types and transport properties of BP can be tuned for the device requirements, hence realizing complementary device applications [19, 58]. In addition, when BP is contacted with different semiconductor, metal, or dielectric materials, different types of interfaces are formed, which affects abundant physical mechanisms for multifunctional devices, including band alignments, carrier transfer, contact barriers, dielectric screening, and so on [29, 59, 60]. By engineering the interface between BP and other materials with strong light-matter interactions, different exotic effects can also be obtained, including anisotropic interlayer exciton, exciton-plasmon polaritons (EPP), plasmon-phonon polaritons, and so on, which can simulate the development of future photonics [61–63]. Last but not least, BP degrades very fast in the ambient environment. Through interface engineering and surface passivation, BP can be protected or modified for practical applications in the atmosphere [64–66].

In this review, we begin with a comprehensive overview of the electronic and optical properties of BP, as well as its degradation mechanism. Then we discuss the different interfaces between BP and other materials and their engineering strategies. The surface modifications and functionalization of BP are also discussed in the section. Subsequently, the interface and surface engineering of BP for different types of applications are demonstrated. Finally, we provide the conclusions and highlight the challenges and opportunities of BP-based optoelectronics and photonics.

2. Physical properties of BP

2.1. Band structure and electronic properties

BP has a layered structure composed of P atoms, in which each P atom is covalently bonded with each of its three adjacent phosphorus atoms [10, 25, 67]. Among them, two P–P bonds form in zigzag (*ZZ*, perpendicular to the pucker) direction, and a bond is formed in armchair (AC, parallel to the pucker) direction, where P atoms are not arranged in the same plane and create the unique puckered structure (see figure 1(a)). Using the GW (G is the Green's function, W is the screened coulomb interaction) calculation, the bond length along the *ZZ* direction is ∼2.24 Å, while the P–P bond length between the two P atoms in the upper and lower sublayer is ∼2.28 Å [25]. Because of the reduced-symmetry orthorhombic lattice structure of BP, the lattice parameter along the *x*- and *z*-directions are different (∼4.58 Å and 3.32 Å, respectively). The unique in-plane anisotropy provides BP with anisotropic physical, electronic, and optical properties [15, 19]. Moreover, BP has a relatively large interlayer distance of ∼5.25 Å, which makes the feasibility of bulk BP exfoliating into few-layer BP. The distance between the top and bottom planes of BP is ∼2.1 Å.

The band structure of bulk BP has long been studied since its discovery in 1914 [69, 70]. According to theory calculations and experimental characterizations, BP has a direct bandgap of ∼0.3 eV at Z-point in the Brillouin zone (see

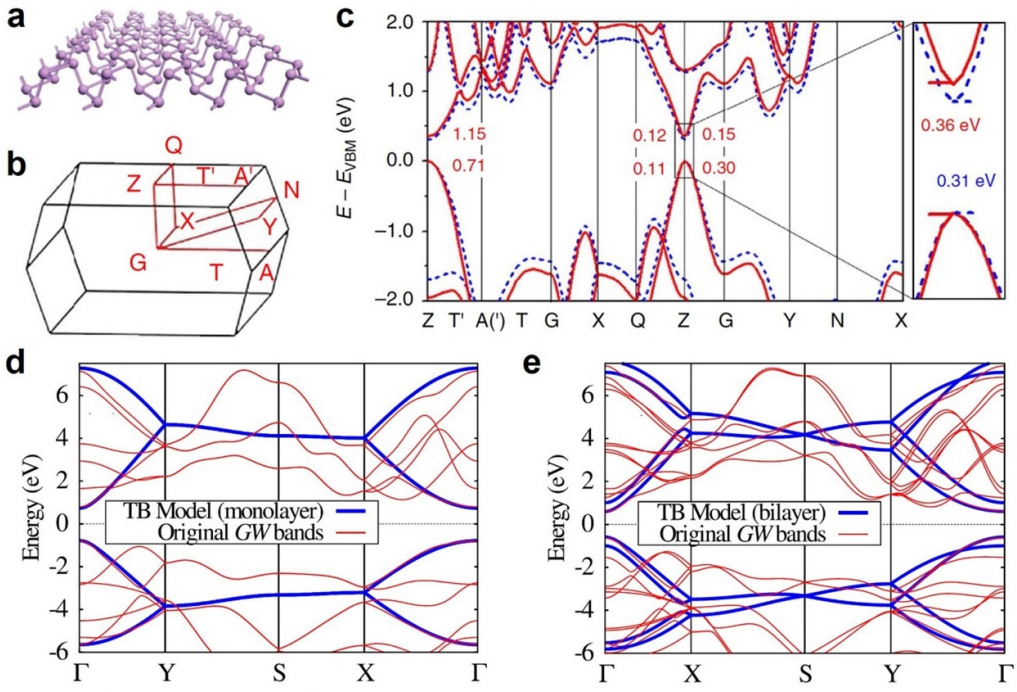

Figure 1. Lattice and electronic band structures of BP. (a) Schematic illustration of the puckered lattice structure of BP. Reprinted from [20] by permission from Springer Nature Customer Service Centre GmbH. (b) Brillouin zone of the primitive cell of BP.(c) Electronic band structure for BP by the mBJ potential (dashed blue line) and the HSE06 functional (solid red line) calculations, respectively. The zoom-in plot in the right of the figure shows the bandgap of BP at z point. (b) and (c) are reprinted from [16] by permission from Springer Nature Customer Service Centre GmbH. (d), (e) Band structures of monolayer (d) and bilayer BP (e), which are calculated by the tight-binding parametrization. Reprinted with permission from [68], copyright (2014) by the American Physical Society.

figures 1(b) and (c)) [16]. When decreasing the layer numbers to few-layers, the interlayer coupling is weaker, resulting in a larger bandgap, and both conduction band minimum (CBM) and valence band maximum (VBM) shift to Γ point in the Brillouin zone [11, 16, 68, 71]. In monolayer BP, the direct bandgap at Γ point is ∼1.6 eV, while in bilayer BP, both valence band (VB) and conduction band (CB) undergo band splitting due to the introduction of interlayer interaction and the companying wavefunction overlap. According to the tight-binding calculation, the bandgap reduces by over 0.5 eV from monolayer to bilayer (as shown in figures 1(d) and (e)). In few-layer BP system, with stronger interlayer interaction and larger dispersion of VB and CB, the bandgap is smaller (∼0.53 eV in five-layer BP). Besides, BP represents anisotropic VB and CB dispersion [16]. The energy band is very steep in the Γ-*X* direction (corresponding to the AC direction in real space), with the carrier effective masses of 0.15 m_0 (hole) and 0.17 m_0 (electron). While in the Γ-*Y* direction (the *ZZ* direction), the energy band is nearly flat, where the hole effective mass is heavily at 6.35 m_0 and the electron effective mass is 1.12 m_0. The results indicate that the carrier transport along AC direction is much faster than along *ZZ* direction.

Due to the direct bandgap feature and steep energy band structure, monolayer BP has high carrier mobility over 1000 $cm^2\ V^{-1}\ S^{-1}$, and the hole mobility is theoretically predicted to be more than 26 000 $cm^2\ V^{-1}\ S^{-1}$. In particular, mechanically exploited BP sandwiched between two hBN flakes shows ultrahigh hole mobility of 45 000 $cm^2 V^{-1}\ S^{-1}$ at cryogenic temperature [14]. The high carrier mobility provides BP with fascinating phenomena such as quantum oscillations and quantum Hall effects, and field effect transistor (FET) applications with high performance.

2.2. Optical properties

2.2.1. Optical absorption. Due to the direct bandgap characteristics regardless of its thickness, BP has tunable optical properties enormously depending on the number of layers. In 2014, Low *et al* systematically calculated the optical properties of bulk BP by the Kubo formula, including optical conductivities and optical absorption with a thickness of more than 4 nm (8 L) [18]. The absorption edge witnesses an increase from 0.3 to 0.6 eV with the thickness decrease, as shown in figure 2(a). When further decreasing the film thickness, the dielectric screening is significant and the excitonic effect cannot be excluded, the enhanced optical absorption appears near the absorption edge. Monolayer and few-layer BP as 2D semiconductors, show step-like absorption characteristics in the single electron interaction picture, and the quasi-particle bandgap E_g would be changed due to the onset of band-to-band transitions [72, 73]. Photoluminescence (PL) spectroscopy has been widely applied to experimentally observing E_g of 2D BP [14, 22, 45, 74, 75]. However, due to the instability of BP and the high sensitivity of PL spectra to defects and doping, the value of E_g reported in these papers are quite different. In 2017, Li *et al* probed the optical bandgap in 1–5 L BP by a simple absorption spectroscopy [20]. The light absorption is insensitive to impurities and defects in 2D

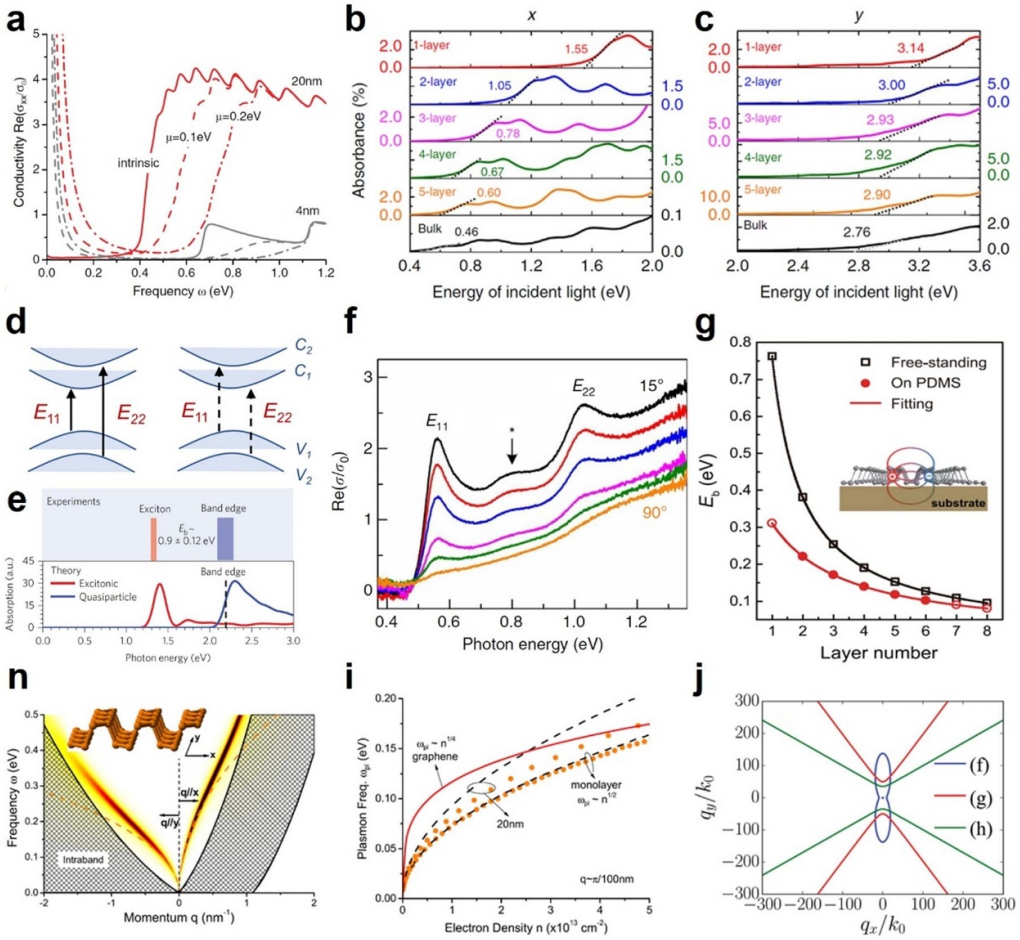

Figure 2. Optical properties of BP. (a) The tunable optical energy gap of multilayer BP with different thicknesses. Reprinted with permission from [18], copyright (2014) by the American Physical Society. (b), (c) Optical absorption spectra for the incident light with the polarization direction along armchair (b) and zigzag (c) directions. The thicknesses of BP vary from one layer to five layers. Reprinted from [16] by permission from Springer Nature Customer Service Centre GmbH. (d)–(g) Exciton effects as well as exciton binding energies in BP. (d) Optical transitions between two quantized sub-bands of BP, based on the quasi-one-dimensional tight-binding model. (e) The model of optical absorption of few-layer BP when considering the exciton resonances, including exciton ground (1s), excited (2s) states, and continuum (step-like) states. Reprinted from [22] by permission from Springer Nature Customer Service Centre GmbH. (f) Real part of the optical conductivity of 6L BP on a quartz substrate with incident light polarizations from 15° to 90°. (g) Theoretical values of exciton binding energies of free-standing BP (black dots) and BP (red dots) on the PDMS substrate, respectively. (f) and (g) are reproduced from [77], CC BY 4.0. (h)–(j) Plasmons in BP. (h) Calculated energy loss dispersion for electron doping in BP of 1×10^{13} cm^{-2} and momentum q paralleled with x (right) and y (left) directions, respectively. (i) Scaling of plasmon frequency with electron concentration of monolayer and 20 nm thick BP, where graphene is for comparison. (j) Distribution of anisotropic plasmons in k surface. (h) and (i) are reprinted with permission from [78], copyright (2014) by the American Physical Society. (j) is reprinted with permission from [68], copyright (2014) by the American Physical Society.

crystals, so absorption spectroscopy is a reliable method for determining the optical bandgap of monolayer and few-layer BP. Combing with the rigorous *ab initio* GW Bethe–Salpeter equation (GW-BSE) calculations, the direct optical bandgap energies evolve from 1.73 eV to 0.75 eV in 1–5 L BP. A rich set of sub-band optical resonances are also revealed, which covering a broad spectral range.

Owing to the orthorhombic crystal structure with low symmetry, BP exhibits highly optical in-plane anisotropy [15, 16]. Qiao *et al* predicted the polarized optical absorption by calculating the dielectric function [16]. The experimental geometry is in figure 1(a), in which the linearly polarized light near-normally illuminates into the sample, and both the sample and the light polarization can be rotated. Two absorption spectra are obtained under the light incidence in the z-direction along with x (armchair) and y (zigzag) directions, respectively, as shown in figures 2(b) and (c). The first absorption peak in figure 2(b) corresponds to the optical bandgap of BP and the absorption edge is at 1.55 eV in the monolayer, which remarkably decreases with thickness. By contrast, under y-polarized light incidence, the cut-off energy is found at 3.14 eV in one-layer BP and its position is insensitive to the thickness, remaining at around 2.76 eV in bulk BP. The dichroism phenomenon is explained by a spatially structural model of wavefunctions in BP. The dipole operator along the armchair direction connects the VB and CB states, which allows the direct inter-band transition, while in the zigzag direction, the direct bandgap process is forbidden and the energy

transition from VB to CB states occurs at much higher photon energy [16]. Lan *et al* and Ling *et al* studied the behavior of anisotropic electron–photon interactions in few-layer BP using angle-resolved light absorption spectroscopy. According to the previous reports, the similar experimental results are obtained by polarized absorption measurement at 1.96 eV. Both the thin (9 nm) and thick (225 nm) BP flakes are measured, in which the imaginary part of the refractive index (i.e. the absorption coefficient) along the armchair direction is significantly larger than that along the Zigzag direction.

2.2.2. Excitonic behavior. Similar to other 2D semiconductors. Few-layer BP has strong many-electron effects of excited states due to the reduced dimensionality and compressed dielectric screening [21, 76]. Therefore, when discussing the band structure of few-layer BP, excitonic behavior as well as the related electron–hole and electron–electron interactions should be considered. In few-layer BP, due to the quantum confinement along the out-of-plane direction, the valence and CBs split into quantized sub-bands (figure 2(d)) [18, 23, 33, 77]. Optical transitions are allowed when sub-bands index has no difference, which leads to the exciton bound state. Figure 2(e) is the illustration of its optical absorption [22]. In free carrier states, the optical absorption of BP is characteristic of step-like features with a quasi-particle bandgap E_g. The transitions from the exciton ground state (1s) to the exciton excited states (2s) lead to new spectral features below E_g. The energy binding energy represents the difference between the lowest energy absorption peak and E_g. Tran *et al* obtained the layer-dependent energy structure of few-layer BP by calculating a GW-BSE [21]. Compared to standard Density Functional (DFT) calculations, the effects of electron–electron interactions are considered in the GW calculation and the underrated quasi-particle bandgap is corrected to 2 eV in Monolayer BP. Furthermore, the exciton binding energy is predicted to largely be at 800 meV, and the lowest-energy absorption peak is 1.2 eV. However, because of the difference between the few-layer BP's optical quality and the effect of substrates, the experimental value of exciton binding energy differs in different reports [20, 22, 24]. For example, according to the first experimental report about monolayer BP's excitons, the exciton binding energy is largely at 900 meV [22], but in another experiment, the value is only 0.1 eV [20]. In 2018, the layer-dependent exciton binding energies in BP from monolayer to over 10-layers were experimentally determined by IR extinction spectra [23]. Here 4L BP is taken as an example. The BP sample is exfoliated on polydimethylsiloxane (PDMS) substrates and the exposure time in the ambient environment is typically <5 min, which promises the high optical quality of BP. A solid and sharp absorption peak (∼20 meV linewidth) is observed at room temperature for armchair light polarization, indicating the huge light-matter interactions at the E_{11} resonance. While for zigzag light polarization, the resonance peak is featureless, originating from unique quasi-one-dimensional (1D) band dispersions of BP. By using a polarization-resolved infrared absorption spectra, the significant anisotropic optical conductivity is observed on a 6L BP sample, as shown in figure 2(f). In addition to the anisotropy, the layer-controlled E_b is also observed in their experiments (figure 2(g)) [77]. For free-standing monolayer BP, E_b is at 762 meV, and the value would be reduced to 316 meV for monolayer BP on PDMS due to the influence of substrate screening [79].

2.2.3. Plasmonic behavior. Surface plasmons in 2D materials provide light confinement and electric-field localization at sub-wavelength scales and can be widely tunable by electrical, which have attracted enormous attention. Low *et al* theoretically reported collective plasmonic excitations in BP [78]. Due to the thickness-dependent optical energy band, BP exhibits tunable optical conductivity with different thicknesses. Figure 2(h) shows the calculated plasmon dispersion in monolayer BP, where the electromagnetic response of BP includes two types of electron motions: the intraband motion (motions of electrons in the CB or holes in the valence band) and the interband transitions (electron transitions between the valence and the CB). As the calculated results in figure 2(i) show, the plasmon frequency (ω) in monolayer BP is determined by carrier density (n), where $\omega \propto n^{1/2}$. While in multilayer BP, due to the interband coupling, the plasmon dispersion relation is modified to $\omega \propto n^{\beta}$, where $\beta < \frac{1}{2}$ instead [80]. The strength of the interlayer screening is between that of graphene and the TMD semiconductors, such as MoS_2. In addition, due to different effective mass along with armchair and Zigzag crystal direction, the plasmonic dispersion shows anisotropic characteristics. The plasmonic propagation along the armchair direction is Landau damped only, which shows long-lived propagation time (figure 2(j)). Corresponding to the reduced symmetry of the atomic arrangement, the hyperbolic plasmon polaritons are predicted to naturally exist in BP, which is the result of the coupling between the inter-band and intra-band optical conductivities [81].

2.2.4. Nonlinear optics. Owing to the quantum confinement, 2D materials commonly have larger nonlinear optical coefficients than their bulk counterparts. Different kinds of the novel nonlinear optical phenomenon have been found in 2D materials, such as strong second-order nonlinear optical effects and second-harmonic generation in MoS_2 [82, 83], WSe_2 [84, 85], and hBN [86], third-order nonlinear optical effects and large Kerr nonlinearity in graphene [87, 88], and so on. Due to the centrosymmetric crystalline structure in intrinsic BP, the second-order nonlinearity is prohibited, but the strong anisotropy and layer-dependently energy band structure allow BP with intriguing third-order nonlinear effects. For example, Third-harmonic generation (THG) has been achieved in multilayer BP samples, demonstrating the substantial third-order nonlinear ($\chi^{(3)}$) process and the promising possibility in mid-infra (MIR) nonlinear optics [89]. Excited by a 1557 nm pump laser, a significant THG signal is obtained in a mechanically exfoliated BP flake (as shown in the microscopy image of figure 3(a)) at the center wavelength of 519 nm. According to the THG mapping results in figure 3(b), the THG intensity is highly dependent on the BP's thickness and sensitive to the wrinkles and boundaries.

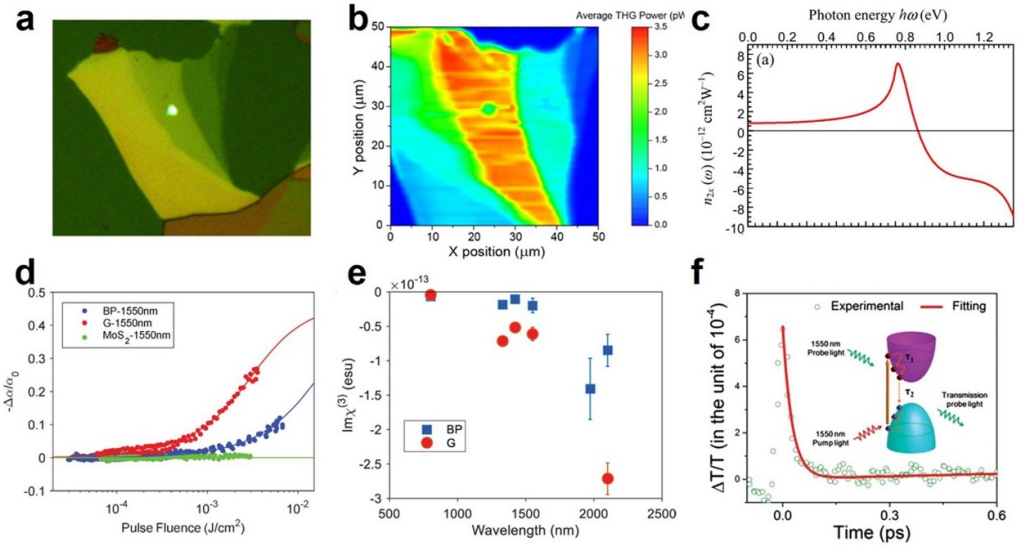

Figure 3. Nonlinear optics in BP. (a), (b) Third-harmonic generation (THG) in a multilayer BP flake. Reprinted with permission from [89], copyright (2017) American Chemical Society. (a) Optical image of the BP flake. (b) THG mapping image excited by a 1557 nm pump laser. (c) Nonlinear refractive index $n_2(\omega)$ of BP along the armchair direction by the numerical simulation, demonstrating the Kerr nonlinearity. Reproduced from [92]. © IOP Publishing Ltd. All rights reserved. (d)–(e) Nonlinear optical absorption of BP. Reprinted with permission from [93], copyright (2016) American Chemical Society. (d) Normalized differential absorptivity of BP, graphene and MoS_2 nanosheets under different incident light fluence. (e) The values of the imaginary part of the third-order nonlinear optical susceptibility Im $\chi^{(3)}$ of BP and graphene measured at different light wavelengths. (f) Transient absorption curve of the BP dispersion at 1550 nm, where the inset illustrates the dynamic carrier process. Reproduced with permission from [48], John Wiley & Sons [© 2015 WILEY-VCH Verlag GmbH & Co. KGaA, Weinheim].

When the thickness is around 15 nm, the THG reaches peak intensity. Two competing mechanisms that the depletion of the THG signal originating from the inherently strong absorption at visible wavelengths and the phase mismatch between the THG and fundamental signal, are responsible for the thickness dependence [34, 90].

The real part of the complex $\chi^{(3)}$ process is responsible for the intensity-dependent refractive index (Optical Kerr effect, $n_2(\omega)$), which has been studied in BP [91, 92]. As the calculation results in figure 3(c), the $n_2(\omega)$ of multilayer BP along armchair direction varies from positive (corresponding to the self-focusing effect) to negative (the self-defocusing of the optical beam) in infra-wavelengths [92]. Furthermore, BP shows anisotropic $n_2(\omega)$ dispersion along armchair and Zigzag directions in which the maximum positive values are about 5.6×10^{-10} cm^2 W^{-1} (in armchair direction) and 6×10^{-11} cm^2 W^{-1} (in armchair direction), respectively. The strong two-photon absorption from visible to infra wavelengths has also been predicted in BP in the paper.

The saturable absorption, originating from the imaginary part of the $\chi^{(3)}$ process, has been systematically investigated in BP from ultraviolet to MIR wavelengths [91, 93–96]. According to Wang *et al* BP dispersions show a large nonlinear absorptive coefficient (α_{NL}) and the value of imaginary part of the $\chi^{(3)}$ process (Im$\chi^{(3)}$), which is comparable to that of graphene, and much more significant than that of MoS_2 dispersions at 800, 1550, and 2000 nm (figures 3(d) and (e)) [93]. In particular, the bandgap of 3–4 L BP is around 0.8 eV, corresponding to a wavelength of 1550 nm. As shown in figure 3(f), 3–4 L BP has ultrafast excited carrier dynamics, where the carrier-to-carrier scattering decay time is only ∼35 fs when the excited light is 1550 nm, which is even faster than that of graphene under the same experimental conditions, indicating the potential of BP as an excellent candidate for telecommunication photonics.

2.3. Degradation

Despite the most stable allotrope in the phosphorus family, few-layer BP still has poor stability in an ambient environment. According to some pioneering studies [97, 98], there are five valence electrons in each P atom, but only three of them form covalent bonds with adjacent atoms. An unbonded lone pair is formed by the other two electrons, which are liable to be degraded in air. Figure 4(a) is the atomic force microscope (AFM) image of freshly exfoliated BP exposed in air, in which small bumps are seen. After a few days, droplet-like structures were observed on the surface.

To explaining the degradation mechanism, there are a large number of papers [67, 99–103]. Favron *et al* firstly investigated the origin of degradation by *in situ* Raman and transmission electron spectroscopies [104], where the effect of visible light in the degradation process is emphasized. Huang *et al* discuss the results of a joint experimental and theoretical study to comprehensively address the interactions of BP with O_2 and H_2O and their effects on the electronic properties and the wetting by aqueous solutions. BP flakes with exposure to air, water with dissolved oxygen, and deuterated water were monitored simultaneously. They found that oxygen plays a crucial role in the chemical modification of BP and in changing its electronic properties, whereas deoxygenated water in the absence of O_2 has a negligible effect. According to research

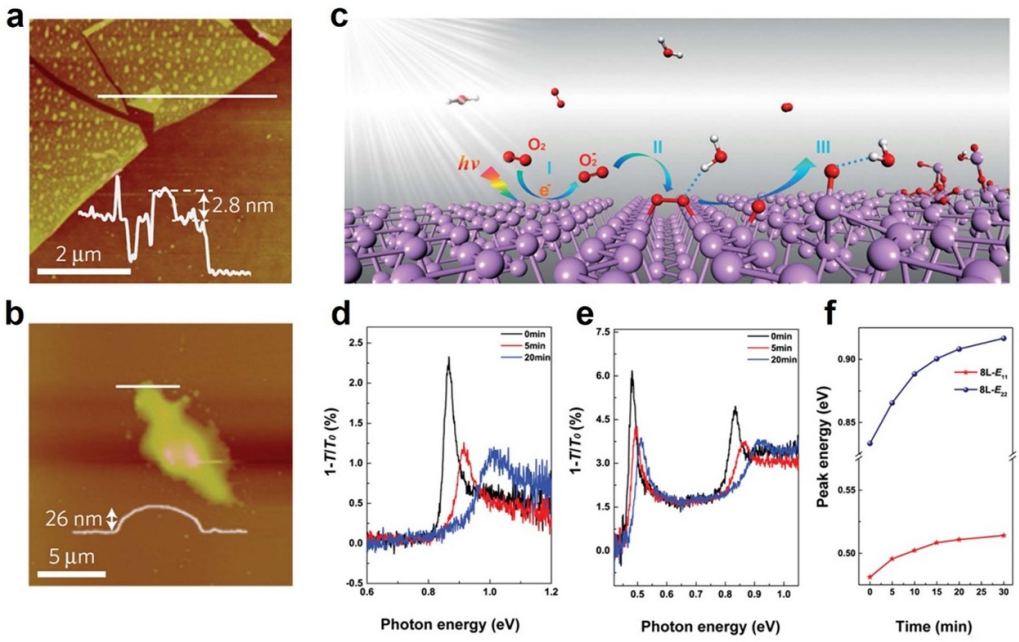

Figure 4. Degradation of BP. (a), (b) AFM image of BP immediately exfoliated on the SiO_2 substrate (a) and placed under ambient conditions after a few days (b). Reprinted from [104] by permission from Springer Nature Customer Service Centre GmbH. (c) Schematic illustration of the light-induced ambient degradation mechanism of BP. Reproduced with permission from [102], John Wiley & Sons [© 2016 WILEY-VCH Verlag GmbH & Co. KGaA, Weinheim]. (d)–(f) Degradation-induced changes in optical absorption spectra as well as electronic band structures of BP. (d), (e) Blueshift of exciton resonances of 3 L (d) and 8 L (e) BP. (f) Changes of E_{11} and E_{22} peak energies as function with exposure time at the ambiance of 8 L BP. Reprinted with permission from [105], copyright (2019) by the American Physical Society.

works [67, 99–103], water, oxygen, and light are combinedly responsible for the chemical breakdown of BP, and even hBN encapsulation was unable to eliminate the degradation.

Wang *et al* studied the degradation-induced changes in the energy structures of few-layer BP [105]. To characterize the impacts of air exposure on the electronic structure of FL-BP, we monitored the evolution of IR and PL spectra of few-layer BP samples in the air over time. All samples were deliberately exposed to air for a specific time and subsequently protected in a chamber by purging nitrogen gas for optical measurements. From the measured IR absorption and PL spectra, the degradation induces a blueshift of all-optical resonances, with shift rates sub-band and layer dependent. They simulate the blueshift of the optical transitions numerically by numerically solving the one-dimensional Schrodinger equation under the effective-mass approximation. The band structure of pristine FL-BP can be approximated as that of an infinite square quantum well. By the same token, the band structure will also be sensitive to the modification of the quantum well profile induced by the oxidation of the surface layer.

3. Interface engineering

For conventional bulk materials, the main approach of changing their physical properties is to modify their chemical bonds or crystalline structure, such as introducing dopant atoms. However, for layered materials like BP, owing to the naturally atomic body thickness, the changes of the material interfaces or interlayer stacking configurations can highly affect materials' properties without changing in-plane chemical bonds. Furthermore, unlike bulk materials with strong covalent or ionic bonds between every neighboring atom, BP has relatively weak interlayer interactions, in which various stacking configurations with different materials (including different semiconductors, metals, and dielectric materials) are allowed. In this section, the engineering strategies of three kinds of BP-based interfaces (BP-semiconductor, -metal, dielectric interfaces) are demonstrated to be not only efficient but convenient for modifying both electronic and optical properties of BP.

3.1. BP-semiconductor interface

3.1.1. Homojunctions. The design of 2D homojunction is a great strategy since the unique geometries and properties, such as homogeneous components, efficient charge transfer at the interface, and perfect lattice matching. Till now, various preparation approaches have been studied for constructing 2D homojunction, including vapor-phase deposition, chemical doping, electrostatic doping, laser irradiation, and so on [106]. In 2015, Yuan *et al* constructed a BP-based vertical p–n junction structure (figure 5(a)) [30]. By ionic gel gating, the surface of the BP flake is heavily n-doped, where electrons are strongly confined, while in the deeper bulk regime, the p-type behavior is preserved. The photogenerated carriers are separated into surface and bulk layers driven by the perpendicular electric field, which significantly enhances the value of photocurrent.

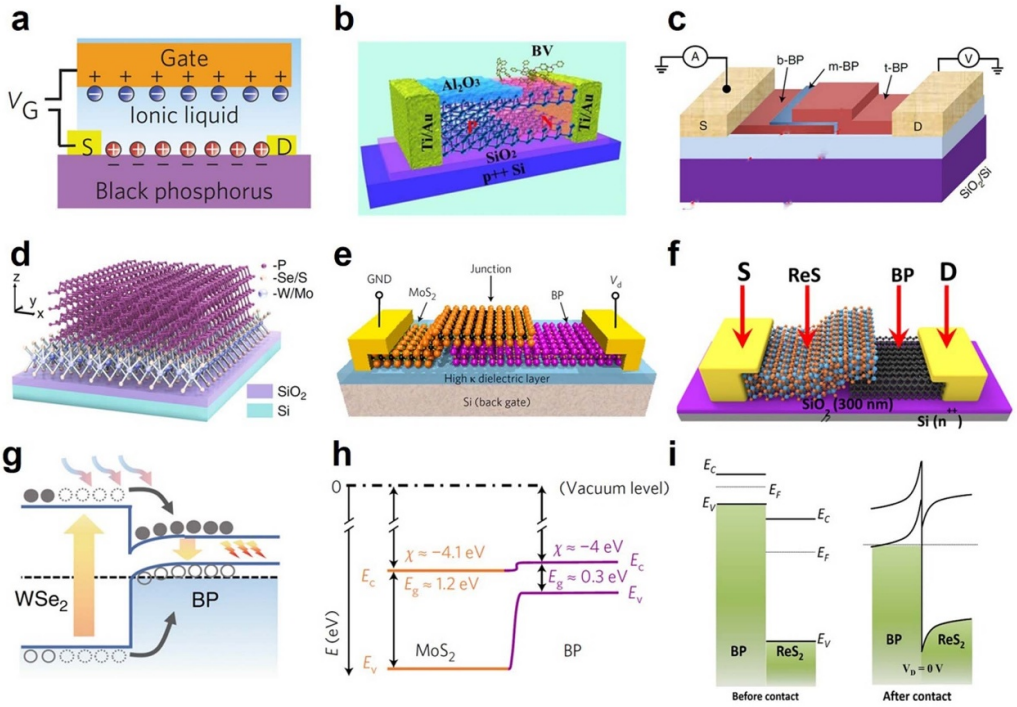

Figure 5. (a)–(c) Schematic diagrams of Homojunctions based on BP. (a) A vertical BP p–n homo-structure based on a typical ionic gel gating configuration. Reprinted from [30] by permission from Springer Nature Customer Service Centre GmbH. (b) A lateral BP p–n structure by chemical doping methods, where Al_2O_3 is the surface hole dopant and BV is the surface electron dopant. Reprinted from [58], copyright (2016), with permission from Elsevier. (c) A trilayer homo-structure based on three BP flakes with orthogonally crystal directions. Reprinted from [109] by permission from Springer Nature Customer Service Centre GmbH. (d)–(i) Schematic diagrams of three different BP-semiconductor heterojunctions and the corresponding energy structures. (d), (g) BP-WSe_2 Type-I heterojunction. Reproduced from [113]. CC BY 4.0. (e), (h) BP-MoS_2 Type-II heterojunction. Reprinted from [29] by permission from Springer Nature Customer Service Centre GmbH. (f), (i) BP-ReS_2 Type-III heterojunction. Reprinted with permission from [114], copyright (2019) American Chemical Society.

The lateral BP p–n junction was also formed by chemical doping methods. Benzyl viologen (BV) as the surface electron dopant was partially doped on the top surface of a few-layer BP [58]. Because the reduction potential of BV is higher than the CBM of few-layer BP, the Fermi-level of BP occurs an upshift to the CB and the carrier type is converted from p-type to n-type. Al_2O_3 with 10 nm thickness was deposited on the other half region of the BP sample as the hole dopant layer and the lateral p–n junction with ambient stability is formed (figure 5(b)). By calculating a modified Schottky diode equation, the homojunction based FET has a low diode ideality factor and small series resistance, showing the advantages compared to other chemically doped p–n structures. Moreover, photodetectors with high detectivity and photovoltaic devices with a power conversion efficiency of ∼0.75% were demonstrated based on the fabricated BP homojunction diode.

A new type of homo-structure is obtained based on twisted BP. According to the first-principles calculations, twisted bilayer BP surprisingly displays isotropic electronic dispersion [107]. In addition, the interlayer couplings in the 90° twisted structure are much weaker than in the individual BP with high anisotropy [107, 108]. Srivastava *et al* systematically studied the twisted trilayer BP (figure 5(c)). Through a standard PDMS stamping transfer technique, a multilayer BP (7–14 L) flake was stacked between two degenerate BP, where the crystal orientation of middle BP is twisted 90° compared to the top and bottom BP flakes. The negative differential resistance and resonant tunneling effects are observed in the orthogonally stacked homo-structure. Furthermore, different from heterostructures, the absence of a physical barrier provides twisted BP with higher current densities and larger peak-to-valley current ratios [109].

3.1.2. Heterojunction engineering. Van der Waals materials display a small lattice mismatch compared to their traditional semiconductor counterparts due to the absence of dangling bonds at the interface. Hence, BP can be staked with other 2D semiconductors with different energy structures flexibly, and different types of heterojunctions are formed at the interface [29, 110, 111]. Such variety in BP-based heterojunctions opens up opportunities for multifunctional and scalable next-generation optoelectronic systems [110, 112].

Experimental evidence of BP-based type-I heterostructure is shown in figure 5(a), where the few-layer BP flake (6 nm) was transferred onto a monolayer WSe_2 thin-film [113]. Since the layer number of BP is over six layers, the direct bandgap is remarkably narrower than that of monolayer WSe_2 (∼2 eV bandgap). From the DFT simulation results, a straddling-gap (type-I) alignment is formed, where BP is regarded as a quantum well and collects the separated electron–hole pairs from the adjacent WSe_2 layer, while WSe_2 as an optical

absorption layer which can enhance the PL of BP at MIR wavelengths. Under the laser excitation of 2.33 eV, the heterostructure sample has a PL peak at ∼3.18 μm, and the PL intensity is 1.65 times that observed in pure BP sample, indicating the efficient energy transfer from monolayer WSe_2 to BP. Furthermore, due to the straddling-gap alignment, the electrons and holes are confined in BP layer, and the PL peak of the heterostructure is at the same position compared to that of the pure BP. Based on the type-I heterostructure, an efficient energy transfer is realized, and the enhancement effect of PL emission is realized.

A typical demonstration of BP-based staggered-gap ((type-II) heterojunction is the BP-monolayer MoS_2 heterojunction [29]. As shown in figure 4, an exfoliated multilayer BP is transferred onto the chemical vapor deposited MoS_2 film, and the overlapped junction region is formed. BP is an inherently p-doped narrow-bandgap semiconductor with high hole mobility, while MoS_2 is an n-type semiconductor with a large bandgap and high electron mobility. The p–n junction is formed in the interface of BP and MoS_2 layers, in which the energy band diagram is in figure 4(e). Under forward, zero, and negative drain bias, the energy barrier between BP and MoS_2 can be adjusted, and different transfer characteristics with high carrier mobility and a large on-off ratio are achieved for multifunctional applications.

The type-III heterojunction has also been realized by choosing BP and ReS_2 flakes, as shown in figure 4(c) [114]. According to the estimating of Kelvin probe force microscopy measurements, the VBM of ReS_2 (∼4.68 eV) is higher than the CBM of BP, manifesting a broken-gap at the interface. The band alignment of the heterostructure at thermal equilibrium is obtained in figure 4(f). A built-in potential barrier (V_{bi}) is formed because the smaller work function of BP compared to that of ReS_2 and electrons transfer from the BP layer to the ReS_2 layer leads to an accumulation layer. Different from the traditional type-I and type-II p–n heterojunctions, no depletion region forms in either side of the type-III heterojunction. By calculations, the width of the hole accumulation layer in the BP region is 43 nm, and that of the electron accumulation layer in ReS_2 is 9 nm. Since the accumulation width in BP is larger than the thickness, BP is demonstrated to be fully accumulated with donors, with the V_{bi} of 0.47 eV. Meanwhile, the ReS_2 layer is partly collected and the V_{bi} is 0.17 eV. Different from the conventional type-I and II p–n heterojunctions, where the diffusion of carriers is temperature-dependent, forward current in the broken-gap band alignments is a temperature-independent tunneling process, making it potentially exploited to create high-speed and integrated devices.

3.1.3. Excitons in heterojunctions. Due to the quasi-one dimensionally electronic dispersion, few-layer BP has unique subband structures, providing exciton-dominated photoexcitation processes. An efficient approach to dissociate excitons into free charges is constructing heterojunctions with type-II band alignments [115]. Figure 6(a) is the schematic diagram that excitons created in the BP layer are dissociated at the interface between BP and P3HT, which greatly enhances free charge carriers. Due to the in-built electric field in the type-II heterostructure, holes flow into P3HT and electrons can be transferred to BP. The photocurrent measurements are performed to indicate the effect of exciton dissociation further. Compared to pure BP, the photocurrent of the BP/P3HT hybrid structure shows a drastic enhancement more than 18.3 times (figure 6(c)). In addition, BP can promote the exciton dissociation of other direct-bandgap semiconductors, in which a significant PL quenching is observed in a BP-MoS_2 heterojunction system [61]. The transfer of interlayer photocarriers between BP and MoS_2 has an ultrafast time of ∼5 ps, which is much shorter than the interband recombination processes of pure BP and MoS_2 [59]. The construction of heterojunctions can promote exciton dissociation and boost the development of ultrafast optoelectronics.

Multiple exciton generation (MEG), where a high-energy photon creates one or more extra electron–hole pairs, is considered a feasible and promising way to overcome the Shockley–Queisser limit and evaluate the light conversion efficiency. According to Zhou *et al* multi-excitons achieved in BP-based MEG systems can be efficiently harvested by constructing heterostructures [116]. They performed transient absorption (TA) measurements for a 4 L BP-1 L MoS_2 heterostructure sample. The MEG occurs within 300 fs when the excitation photon energy is more than two times the bandgap of 4 L BP. Based on theoretical calculations, the type II band alignment is formed, and the photoinduced electrons in BP flow into MoS_2 (figure 6(d)). According to the 2D plot of TA spectra in figure 6(e), the photoinduced bleaching of A and B excitons of monolayer MoS_2 is achieved while the excitation energy is lower than the bandgap of monolayer MoS_2, indicating the carrier transfer from BP to MoS_2. The electron density, as well as transfer process, is probed using photoinduced bleaching kinetics of MoS2. Interestingly, the transmission difference at the excitation energy of 2.25 eV is 1.32 times that of 1.36 eV under the same absorbed photon density, which is coincident with the contribution of MEG, confirming the multielectron transfer process (figure 6(f)).

Like bulk quantum well structures, interlayer (or indirect) excitons can also be hosted in 2D heterostructures [117]. These excitons have a prolonged lifetime and are controllable by electric fields, so they are of particular interest. Till now, studies on interlayer excitons have mainly focused on TMD materials and gapped graphene [118–120]. BP has a tunable and direct bandgap, which can be an ideal platform for interlayer excitons. However, there have been no experimental studies about BP-based heterostructures for interlayer excitons till now. Chen *et al* designed BP-GeS and BP-hBN heterojunction systems and predicted their exciton properties [121]. Both of these systems support the existence of bright interlayer excitons. In addition, in the BP-GeS heterostructure, the exciton effective mass is changed due to the strong hybridization, and the exciton lifetime is prolonged at room temperature. While in the BP-hBN-BP heterostructure, the hBN decouples the BP layers and allows the appearance of low energy dark excitons with very small oscillator strengths.

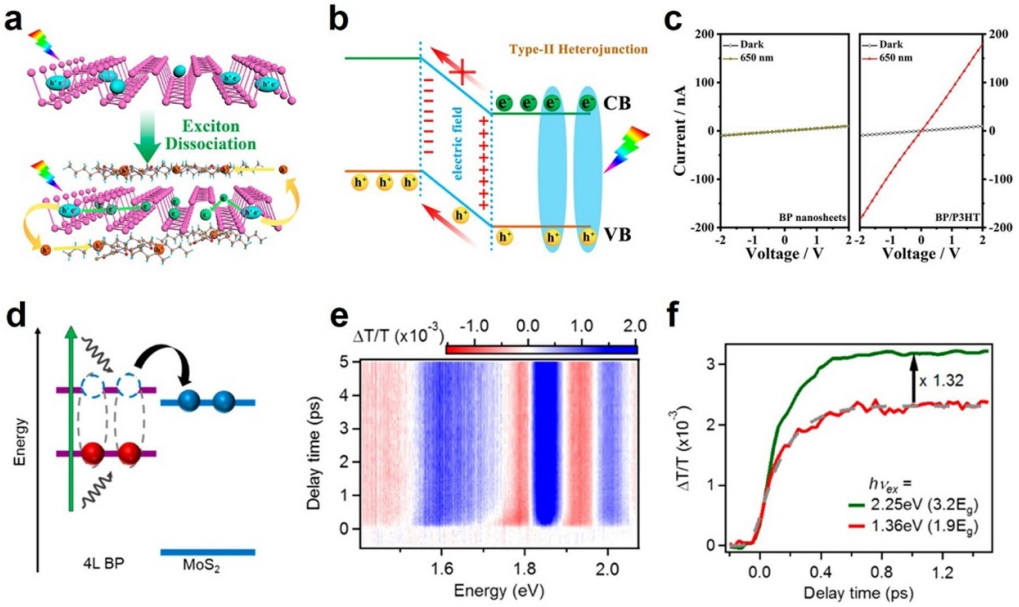

Figure 6. Exciton generation, dissociation, and harvesting mechanisms in BP-semiconductor heterostructures. (a)–(c) Exciton dissociation at the interface of BP/P3HT and the enhancement of photocurrent generation. Reprinted with permission from [115], copyright (2019) American Chemical Society. (a) Schematic diagram of the transfer of electrons and holes at the BP/P3HT interface. (b) Migration of electrons and holes adjacent to the p–n heterojunction. (c) I–V characteristics of BP (left) and BP/P3HT heterostructure (right) under dark and 650 nm light illumination conditions reflect the enhancement of photocurrent in the heterostructure. (d)–(f) Multiple exciton generation and harvesting in BP-MoS_2 heterostructure. Reprinted with permission from [116], copyright (2020) American Chemical Society. (d) Theoretically calculated band alignment indicates the generation of multiple excitons from 4 L BP and the exciton dissociation by interfacial electron transfer to MoS_2. (e) Transient optical absorption spectra of heterostructure under 1.36 eV excitation. (f) Transient absorption kinetics of MoS_2 A exciton within 1.5 ps time scale under 1.36 and 2.25 eV excitation energies, respectively.

3.2. BP-metal interface

3.2.1. Metal-semiconductor contact. The contact engineering between 2D semiconductors and metal electrodes also plays a vital role for optoelectronic devices. Traditionally, the metal is evaporated onto the contact area of the 2D functional layer, which is based on the non-van der Waals junction interface. The barrier height in metal-semiconductor contact is mainly decided by semiconductor electron affinity and metal work function. By aligning suitable metal and semiconductor layers and designing band edges, the barrier height and the contact resistance can be reduced, and the optoelectronic performance is effectively modified. Figure 7(a) is the schematic diagram of a BP-based FET device, where different metals were adopted as electrodes [122]. The BP/metal interface shows the typical Schottky barrier behavior, but with different contact metals, the barrier height and contact resistance are significantly different. As shown in figure 7(b), the contact resistance of BP/ Pd interface ($1.75 \pm 0.06\ \Omega$ mm at -40 V gate voltage) is much smaller than that of BP/ Ni interface ($3.15 \pm 0.15\ \Omega$ mm at the same gate voltage). Metal Pd has a higher work function ($\sim$5.4 eV), making it easier to inject holes from the metal into the VB of BP and reducing contact resistance [123, 124]. By gating modulating the two Schottky barriers, the device can be alternated from p-type to n-type characteristics.

Another strategy for constructing metal/semiconductor interface is using 2D semimetals as graphene and bismuth [125] as the buffer layer or electrodes. Unlike the traditional processes, the van der Waals heterogeneous contact technique avoids the damage of the evaporation process without chemical bonding and reduces the Schottky barrier width. Figure 4(c) is the BP-based LED device, where two graphite films sandwich the BP flake with 87 nm thickness [46]. A high current up to 6.7 mA can be injected into the BP flake with $\sim$1200 μm^2 region, indicating the narrow barrier width (figure 7(d)).

3.2.2. Enhanced light-matter interactions. Although few-layer BP has extraordinary optical properties, an inherent drawback is their weak light absorption due to the thinness. Constructing hybrid nanostructures with metals is an effective approach for enhancing light-matter interactions. For example, the effects of gold-based nanostructures have been studied to boost light absorption and the IR light emission in BP [126]. The schematic illustration is shown in figure 7(e), where the Al_2O_3/Au substrate acts as a spacer/mirror structure and BP is stacked on the metallic mirror. Then the periodically arranged array of T-shaped Au nano-antennas is placed on the top of BP. According to the simulation results, the thickness and length of each nano-antennas are 30 and 400 nm, respectively. The antenna gap is 40 nm, which is aligned along the armchair direction of BP. Due to the light confinement of the metallic substrate and the effective manipulation of the Plasmonic nano-antennas, the light absorption of BP achieved a huge enhancement at the localized surface plasmon resonances wavelength ($\sim$3.08 μm, corresponding to the

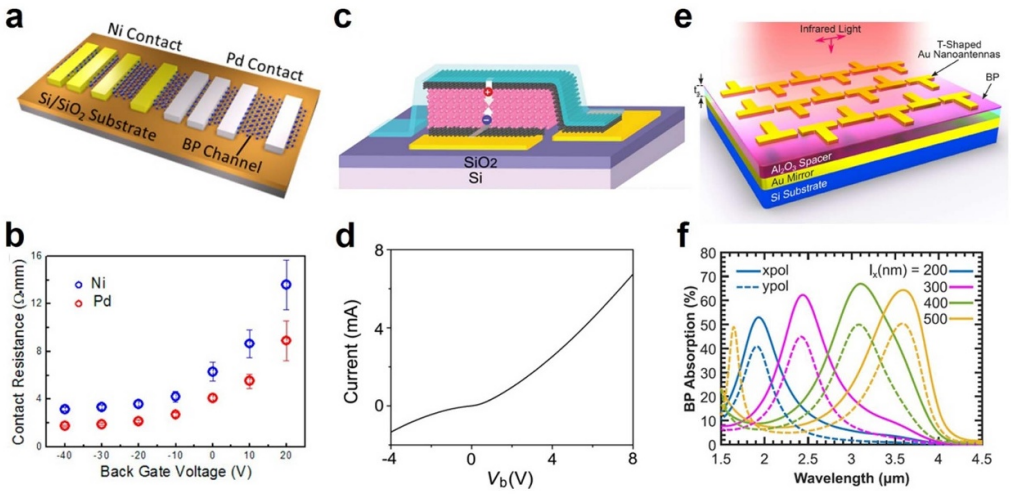

Figure 7. Interface engineering between BP and metals. (a), (b) Ni/Au and Pd/Au contacts depositing on BP flakes. Reprinted with permission from [122], copyright (2014) American Chemical Society. (a) Schematic illustration. (b) Contact resistance characteristics with different back-gate voltage. (c), (d) Graphene as electrodes for BP functional layer. Reprinted with permission from [46], copyright (2020) American Chemical Society. (c) Schematic illustration of a BP flake sandwiched by two graphite films. (d) Typical I–V characteristics of the graphite-BP-graphite device. (e), (f) Metals on BP for light–matter interaction enhancement. Reprinted with permission from [126], copyright (2021) American Chemical Society. (e) T-shaped Au nano-antennas with polarization-tailoring alignments on BP. (f) Enhanced optical absorption of BP for *x*- and *y*-polarized light incidence.

0.3 eV bandgap of BP). The spontaneous emission rate of BP is also accelerated. Furthermore, the T-shaped configuration of Au shows Polarization-Tailoring characteristics that the *y*-polarized illumination light is rotated in the gap and around the T legs. The surface charge oscillations along *y*-direction are converted to the T arms along the *x*-direction, so a nearly isotropic light absorption in BP is created, as shown in figure 7(f). From the Finite-difference time-domain calculation, the light absorption along *x*- and *y*-polarized directions of BP achieves a huge enhancement of 185 and 16 times, respectively.

As the thickness of BP decreases to atomic layers, the excitons show great electromagnetic response and strong coupling capability, in which the energy exchange rate between BP and metals is faster than the respective dissipation rate. The separated exciton and plasmonic states would be coupled into the EPP state [127]. According to Liu *et al* the EPP coupling and Rabi splitting at the interface between monolayer BP and Au is theoretically predicted [63]. They constructed a Drude model of the dielectric function of 1 L BP, where the exciton emission is at 1.73 eV with the binding energy of ∼270 meV. By a transfer matrix of the optical characteristics of BP and Au, the EPP coupling occurs under the particular excitation angle and distance of a prime. The strong EPP coupling in the BP-Au heterostructure platform will have application potentials, including optical sensors, photodetectors and slow-light devices [128, 129].

3.3. BP-dielectric interface

3.3.1. BP natural quantum wells and electro-optical effect.

Quantum well semiconductors, such as III–V quantum wells and Si/SiGe quantum wells, have been widely studied to have superior electro-optical properties [130–132]. The quantum-confined Stark effect acts as the dominant electro-optical effect in semiconductor quantum wells, where the absorption band edge of III–V heterostructures experiences a red-shift under a transverse electric field. When few-layer BP is placed on the SiO_2 dielectric layer, it can be regarded as a natural quantum well structure, in which the quantum-confined Stark effect is also presented. According to Liu *et al* the giant Stark effect coefficient is achieved in electrostatically gated few-layer BP, where a semiconductor-to-metal transition is allowed under a low critical field (∼0.68 V nm^{-1} for ten-layer BP) [133].

In addition, other than traditional quantum wells, most of which cannot be operated beyond the telecommunication spectrum (0.8–1.7 μm), few-layer BP shows excellent electro-optical characteristics in the MIR frequencies [33]. An intrinsic 5 nm BP film was exploited on the SiO_2 substrate. The upper air and bottom oxide interfaces make BP a quantum well structure. Applied an out-of-plane electric field, the evolution of the energy band diagram is shown in figure 8(a). The bandgap of intrinsic 5 nm BP is around 0.62 eV, which is determined by the energy levels of the first valence and conduction sub-bands, respectively. When a positive gate bias is applied, the field-induced quantum-confined Franz–Keldysh effect leads to the upshift of the Fermi level E_f, where the band bending occurs in the BP quantum well and the electron and hole sub-bands become closer in energy [19]. On the other hand, 2D electron gas becomes more degenerate at the BP-oxide interface by the induced electron carrier density N_s, leading to the upshift of the Fermi level E_f and the broadening of the bandgap, which originates from the Pauli-blocked Burstein–Moss shift (BMS), as shown in figure 8(b). The two mechanisms make optical bandgap of gate biased BP may undergo blue-shift, red-shift, or bidirectional-shift, which cannot be realized in graphene and traditional III–V semiconductors.

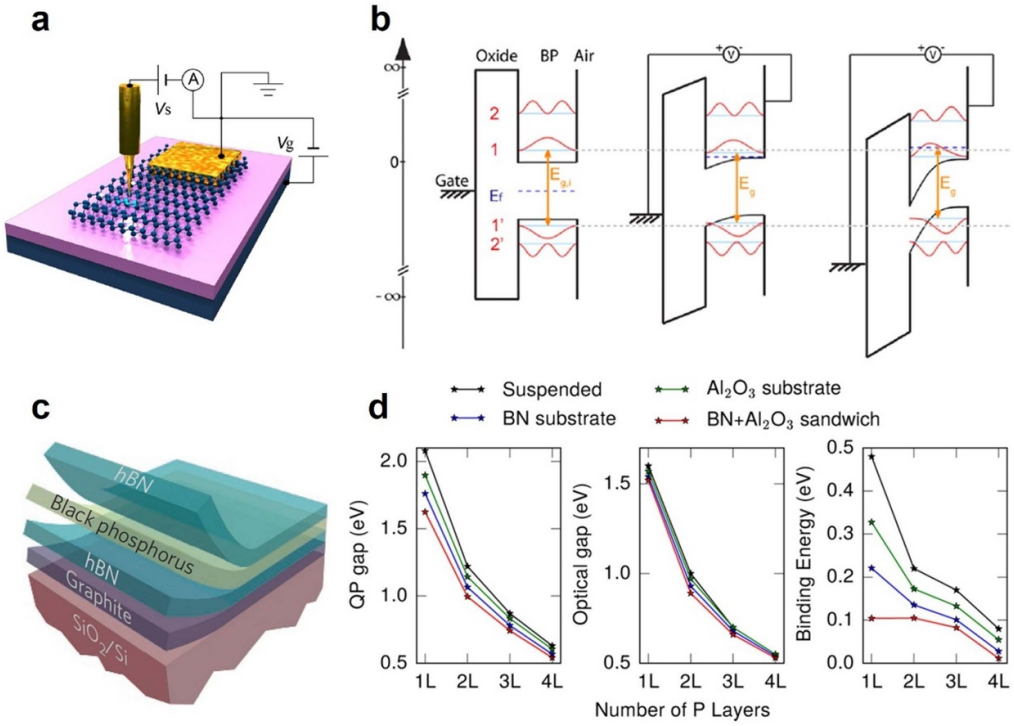

Figure 8. Interface engineering between BP and dielectric materials. (a) and (b) BP between oxide and air layers as natural quantum wells for electro-optical effects [33, 133]. (a) Schematic diagram of a BP flake on SiO_2 substrate as a gate-tunable device for electro-optical effects. Reprinted with permission from [133], copyright (2017) American Chemical Society. (b) Energy band structure illustrating the change of bandgap of BP natural quantum wells under intrinsic, QCFK, and BMS regimes, respectively. Reprinted with permission from [33], copyright (2016) American Chemical Society. (c) Schematic diagram of BP sandwiched by two hBN layers. Reprinted from [135] by permission from Springer Nature Customer Service Centre GmbH. (d) Exciton characteristics including quasi-particle gaps, optical gaps, and binding energy in 1–4 L BP with and without dielectric encapsulation. Reprinted with permission from [60], copyright (2017) American Chemical Society.

Besides the optical bandgap as well as optical absorption changes, the optical anisotropy in few-layer BP is also tunable by an externally applied field, in which the highly anisotropic absorption is transformed to a nearly isotropic feature [134]. Since the disallowance of inter-subband optical transitions along the Zigzag direction of BP, the influence of BMS shows a significant difference between in armchair and in Zigzag direction. The quantum-confined Stark effect is also anisotropic in BP. When sandwiched BP between two dielectric layers (such as SiO_2 and Al_2O_3) and applied a symmetry-breaking electric field, both linear dichroism and birefringence are electrically controlled.

3.3.2. Dielectric screening and many-body effects. It is known that the dielectric screening between 2D semiconductors and the surrounding environment plays an important role in the quasi-particle gaps and exciton-binding energies. According to previous reports, when other fused silica or oxides materials, including SiO_2, quartz, Al_2O_3, and hBN are used as substrates or capping layers, the optical gap of monolayer BP is experimentally obtained ranging from 1.3 eV to 1.73 eV, where the bandgap shifts raise from the dielectric screening-induced effects [60, 135].

By calculating the GW-BSE equations, Qiu *et al* systemically studied the effects of the encapsulating environment in few-layer BP and their calculation matches well with the previous experimental results [60]. At first, they modeled a nearly commensurate supercell that monolayer BP is sandwiched between (0001) Al_2O_3 substrate and hBN capping layer (figure 8(c)). Different factors such as the relaxed distance between BP, substrate and the capping layer, lattice mismatch, and the anisotropic effective mass along different directions are considered in the calculation. The changes of the QP gaps, optical gaps, and exciton binding energies of 1–4 L BP under the effects of the substrate and encapsulation are depicted in figure 8(d). When monolayer BP is sandwiched by hBN and Al_2O_3, the QP gap reduces by 0.48 eV and the exciton binding energy decreases by as much as 70% (from 0.48 to 0.14 eV). BP is more sensitive to the surrounding environments than TMDs, owing to BP's small intrinsic dielectric constant (a static dielectric constant of six for BP and 13–16 for bulk MoS_2). Similarly, in 4 L BP, the renormalization of the QP gaps (by 0.09 eV) and exciton binding energies (from 0.07 to 0.01 eV) is achieved by the encapsulation.

4. Surface engineering

Surface engineering strategies, such as surface modification by introducing dopant atoms, absorbers and impurities, and plasma etching, have long been studied in conventional bulk materials and have now been widely developed in 2D materials. For few-layer BP, the two most inherent shortcomings

are relatively low electron mobility and poor air stability. Both of these two shortcomings can be optimized through surface engineering, as discussed in this section.

4.1. Charge transfer doping

BP is inherently an ambipolar semiconductor with strong asymmetry between electron and hole transport, where both the mobility and concentration of electrons are orders of magnitude lower than that of holes, limiting the applications in optoelectronics [136, 137]. Since the transport behavior of BP is sensitive to surface impurities, absorbates, and adatoms, surface functionalization is a practical approach to tune the p- or n-doping level of BP. Unlike the conventional substitutional doping or plasma treatment, surface functionalization as a nondestructive doping scheme, does not introduce a significant number of defects or even destroy the crystal structure of the underlying semiconductors. In 2015, Du *et al* reported the surface functionalization of BP with two metal oxides, Cs_2CO_3 and MoO_3 [136]. As a substantial electron donor, Cs_2CO_3 significantly increases the electron concentration in BP, thereby enhancing electron mobility. As shown in figure 4(a), with the increase of the n-type doping level, the transfer characteristics of BP have a transition from hole-dominated to electron-dominated behavior. While in MoO_3 covered BP, owing to the extremely high work function of MoO_3 in a high vacuum, a giant p-doping effect is observed. The photoresponsivity of BP-based photodetectors was increased more than four folds for both MoO_3 and Cs_2CO_3 doping cases.

Following the functionalization study, some dopants such as Cu, Al, K, BV, and self-assembled layers have been used to modulate the electronic and optical properties of BP [19, 42, 138–142]. For example, by contacting Cu adatoms, the controllably n-doped few-layer BP is achieved, lowering the threshold voltage for n-type conduction [138]. Both Cu adatoms bond to the top surface and Cu atoms are intercalated into the few-layer crystal. According to the DFT calculation, a massive Fermi level shift is observed, where the donated electron originates from the Cu^{4s} shell. In the Cu as configuration, the bandgap is reduced to 0.09 eV due to an internal electric field, while for the intercalated Cu_{int} configuration, besides the n-type doping the distance between the two BP layers increases, decoupling the system into two BP bilayers, leading to a rise in the bandgap from 0.18 to 0.32 eV.

Al atoms have been doped at the surface and the intercalated site of few-layer BP nanosheets, which induce n-type conductance [42]. Due to the hybridization of the Al atom with the lone electron pair in phosphorus atoms, the binding energy is large, which leads to large outward and in-plane atomic displacements of phosphorus atoms around the Al dopant. The Fermi level in the Al-BP system shifts upwardly into the CB.

Organic absorption on van der Waals materials has long been studied and shows a pronounced doping effect [64–66, 143–145]. Dopants with a bipolar pole or low redox potential lead to the n-doping effect. For example, $-NH_2$ containing organics has long electron pairs to withdraw holes from the host material [143].

In 2016, Hersam *et al* reported a pioneering work on the covalent functionalization of BP via aryl diazonium chemistry, triggering the research hotspot of chemical functionalization of BP [64]. By reacting few-layer BP with different aryl diazonium salts, namely 4-nitrobenzenediazonium (4-NBD) and 4-methoxybenzenediazonium tetrafluoroborate salts, BP was successfully passivated by covalently attaching the aryl groups through P–C bonds. As a result, phosphorus atoms are four-coordinate bonded, with one lone pair of the electrons forming P–C bonds; thus, its reactivity with oxygen is inhibited.

Molecule doping is a flexible and effective method for optimizing the electronic properties of 2D materials [58, 145]. Yu *et al* employ BV as the surface electron dopant on the top layer a (p-type) few-layer BP flake and achieve an ambient stable, in-plane P–N junction [58]. N- and p-doping of BP was achieved with 3-amino-propyltriethoxysilane (APTES) and octadecyltrichlorosilane (OTS). The functional groups in APTES (NH_3-) and OTS (CH_3-) have negative and positive charges, respectively, which are able to adjust the carrier density in the BP channel. The photocurrent of the APTES-doped BP photodetector decreased from 77.9 to 65.9 nA μm^{-1}. Conversely, for OTS-doping, the recombination rate of photocarriers appears to be reduced in the BP channel. As a result, the photocurrent increased from 133 to 187 nA μm^{-1} after OTS doping.

Covalent functionalization of BP generally has a limited degree of functionalization, and in some cases, the grafted functional groups may even degrade the electronic properties of BP. There are several non-covalent functionalization approaches of its 2D surface that were pioneered in order to protect BP from degradation under ambient conditions. For example, Hirsch *et al* reported a noncovalent hybrid of BP with 7,7,8,8-tetracyano-pquinodimethane (TCNQ) and perylene bisimide via van der Waals interactions [66]. The ambient stability of BP was enhanced significantly. Adsorption of stable molecules on the surface of BP by electrostatic interactions has been developed as an alternative strategy to protect BP.

4.2. Improvement of ambient stability

As discussed in section 2.3, the unbonded lone pairs of phosphorus atoms is easily reacted with oxygen, few-layer BP suffers from oxidization and degradation when exposed to air. For effectively improving the air stability of BP, the most two common approaches are physical coating and chemical functionalization. Plasma etching and thermal annealing have also proven to be effective for preparing stable BP. Table 1 summaries variety of passivation techniques of BP as well as characterization methods.

Physical coating or covering can serve as a physical barrier to encapsulate BP, which avoids the environmental reaction of BP's lone pair of electrons. In 2014, Wood *et al* deposited 10 nm thick Al_2O_3 onto a 9 nm thick exfoliated BP flake. The inorganic coating method effectively suppresses the ambient degradation of BP and the as-prepared FET maintained high On/Off ratio and mobility over two weeks. Followed by the

Table 1. Passivation techniques for improving air stability of BP. The monitored time only refers to the duration it is monitored using characterization techniques, which is not the maximum survival time of BP.

Passivation technique	Type	Monitored time	Characterization method	References
ALD of AlO_x overlayers	Physical coating	14 days	AFM and charge transport measurements	[27]
Al_2O_3/Teflon-AF encapsulation		4 months	Charge transport measurements	[147]
PMMA coating		19 days	Raman measurement	[148]
Organic monolayers PTCDA via vdW epitaxy		—	Classical molecular dynamics (MD) simulations	[149]
hBN-BP-hBN sandwiched configuration		150 h	Charge transport measurements	[150]
Noncovalent functionalization with 7,7,8,8-tetracyano-p-quinodimethane (TCNQ)	Chemical functionalization	2 days	Raman, AFM, FTIR, STEM-EELS	[151]
Noncovalent functionalization with 1-methyl-2-pyrrolidone (NMP)		8 days	AFM, Raman, DFT calculations	[152]
Covalent functionalization with 4-nitrobenzene-diazonium (4-NBD)		10 days	AFM, XPS, Raman, charge transport, DFT calculations	[64]
Covalent functionalization with Titanium sulfonate ligand (TiL_4)		3 days	NMR, Raman, XPS, AFM	[65]
Self-assembled octadecyltrichlorosilane (OTS)		28 days	XPS. Raman, charge transport	[144]
O_2 plasma etching + Al_2O_3 coating	Combined passivation	2 months	Phase-shifting interferometry, PL, Raman	[146]
O_2 plasma etching + hBN covering + rapid thermal annealing		7 months	STEM, PL, Raman	[153]

research, different capping methods have been studied, such as organic coating, Al_2O_3-organic encapsulation and 2D flakes. In addition to the considerable protecting ability, the most merit of physical coating methods is that the intrinsic properties of BP can be highly preserved because any chemical process is not involved in the whole passivation processes.

Chemical functionalization is another effective way to enhance the air stability of BP. A pioneer work is the noncovalent functionalization of BP's 2D surface with TCNQ. The stable hybrids are formed between BP and TCNQ molecules and electron transfer occurs from BP to the organic layer, which can highly stabilize the BP flake but also affects BP's mobility. The covalent functionalization of BP is developed as an alternative strategy to protect BP. For example, Hersam's group developed a wet chemical approach in which aryl diazonium 4-NBD is covalent modified with 10 nm thick BP. An invariant morphology is exhibited in BP over three weeks of ambient exposure and the electronic properties is controllable due to the covalent bonds between BP and the passivation component. However, the as-protected BP still has low functionalization degrees in this way, and a clear spectroscopic fingerprint is absent for characterizing the covalent functionalization degrees. In 2020, by introducing insert solvent and non-time-consuming statistical Raman Spectroscopy, Wild *et al* established the systematic quantification method to dramatically increase the functionalization degree of methylated BP. Both P–C and C–H covalently vibrational modes are exhibited from the spectroscopy analysis, indicating the construction of a phosphine like P_2P-CH_3-species. The functionalization degree is quantitated and highly at 4.7% for NaP_4 and 7% for KP_6 BPICs.

The combination of physical and chemical passivation can furtherly enhance BP's air stability. For example, Pei *et al* fabricated air-stable phosphorene flakes through oxygen plasma etching and the following Al_2O_3 coating (figures 9(d)–(f)). Using the oxygen plasma etching method, P–O covalent bonds are formed on the BP surface and the P_xO_y capping layer is produced as a protective coating. Then a 5 nm thick Al_2O_3 layer is deposited as an extra passivation layer. As shown in figure 9(f), the BP flake capped with P_xO_y and Al_2O_3 protected layers maintains clean topography over two months under air exposure. Followed by this work, Li *et al* developed a systematic strategy by combing O_2 plasma etching, boron nitride passivation, and thermal annealing process. The rapid thermal annealing method can effectively reconstruct the surface defect and amorphous P_xO_y and maintain BP's intrinsic properties. According to their PL degradation results, the PL intensity of their BP sample remains at ∼80% of the original intensity after 209 days (seven months) under ambient environment, indicating that the combined passivation strategy is effective for air-stable and high-quality BP samples.

5. Applications

Nowadays, different kinds of high-performance BP-based devices have been developed, including photodetectors, LEDs, electro-optic modulators, all-optical modulators, and so on. Interface and surface engineering play an essential role for all of these devices. For example, the responsivity can be improved, and the working wavelength can be broadened by constructing P–N junctions in BP-based photodetectors.

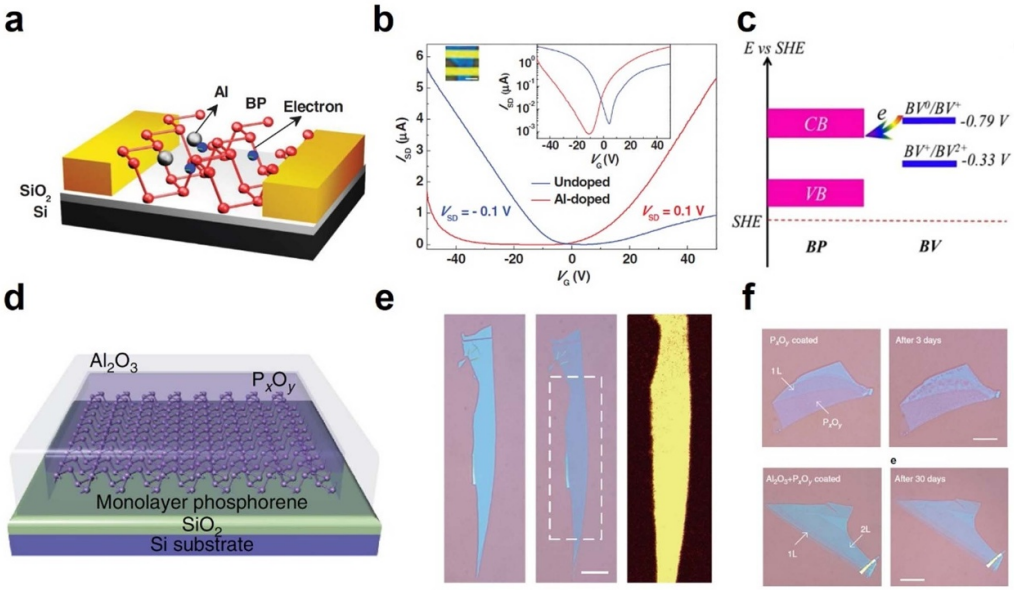

Figure 9. Surface engineering of BP. (a), (b) Al-doped BP as n-doped functional layers for transistor characterizations. Reproduced with permission from [42], John Wiley & Sons. [© 2017 WILEY-VCH Verlag GmbH & Co. KGaA, Weinheim]. (a) Schematic diagram that shows Al atoms as electron dopants for the BP host lattice. (b) Transfer characteristics of BP transistors, which indicate the transform from p-type to n-type of BP when doping Al atoms. The inset is the same plotted data but using a logarithmic scale. (c) Energy band alignment of BP and BV, which exhibits the n-type chemical doping effect of few-layer BP. Reprinted from [58], copyright (2016), with permission from Elsevier. (d)–(f) Oxidation and surface coating for ambiently stable BP. Reproduced from [146]. CC BY 4.0. (d) O_2 plasma etching and Al_2O_3 coating on a BP flake. (e) Optical images of fresh exfoliated (left) and O_2 plasma etched (middle) BP, as well as the PL mapping image. (f) Visual images of an O_2 plasma etched BP flake before and after three days and a $P_xO_y + Al_2O_3$ coated BP flake before and after 30 days.

Through designing a BP–WSe_2 based straddling-gap alignment, carriers are efficiently confined in BP, and the PL intensity of BP-based LEDs achieves a significant enhancement. By surface coordination, BP with good air stability for air-stable optoelectronic and photonic devices. This section focuses on the interface and surface engineering strategies in these promising applications.

5.1. Photodetectors

Photodetectors are optoelectronic devices that can capture the light signal and convert it to an electric signal, which have been indispensable devices in modern photonics and optoelectronics. The moderate and direct bandgap of BP makes it suitable for photodetection applications, especially in near-infra (NIR) and MIR wavelengths [26, 32, 39, 154–156]. BP-based photodetectors with different structures and working modes have been studied, showing promising device performance such as ultrahigh responsivity and fast response time [30, 37, 38, 110, 157–161]. Furthermore, the unique anisotropy makes BP sensitive to light polarization and the possibility for polarization-sensitive detection [30, 155]. Figure 10(a) is the optical image of a BP-based polarization-sensitive detector, where a ring-shaped gating electrode is used for excluding the influence from the geometric edge at the BP-metal interface [30]. From the spatial photocurrent mapping image at 1550 nm (figure 10(b)), the device works at photoconductive mode and strong photocurrent for AC polarization is observed in BP between two electrodes. By contrast, the photocurrent for *ZZ* polarization from 400 nm to 1700 nm is at least an order of magnitude smaller than that for AC polarization, demonstrating the linear dichroism of the device. Shortly after, Bullock *et al* realized the linearly polarized detection of BP at MIR waveband by constructing a vertically stacked BP-MoS_2 heterostructure. The MoS_2 layer acts as an electron-selective contact which allows the flow of electrons while blocks the flow of holes from BP to the top electrode and BP has proved to be promising for polarized mid-IR detection [159].

Tunable BP-based MIR photodetectors have been realized by designing a dual-gate device configuration on the interface of BP [32]. By supplying a high back-gate voltage and a considerate top-gate voltage, strong photoresponse at room temperature is observed with an extrinsic responsivity of 518, 30, and 2.2 mA W^{-1} at 3.4, 5, and 7.7 μm, respectively. The light absorption edge as well as photoresponse witnesses a significant redshift, originating from the shift of the charge-neutrality position of BP and the Franz–Keldysh effect. Yuan *et al* improved the dual-gate transistor structure above, where the top gate layer uses monolayer graphene to replace metals, and the thickness of the BP functional layer is increased to 13 nm (see figure 10(c)) [162]. The transparency of graphene ensures more than 99% transmission of incident light at MIR wavelengths, while the thickness of 10–15 nm of BP is a compromising result considering the light absorption and the free-carrier screening effect. A matrix learning process from a temperature tunable blackbody source allows an ultra-compactly optical spectrometer to be realized in the spectral range from 2 to 9 μm. Figure 10(d) is the source-drain current

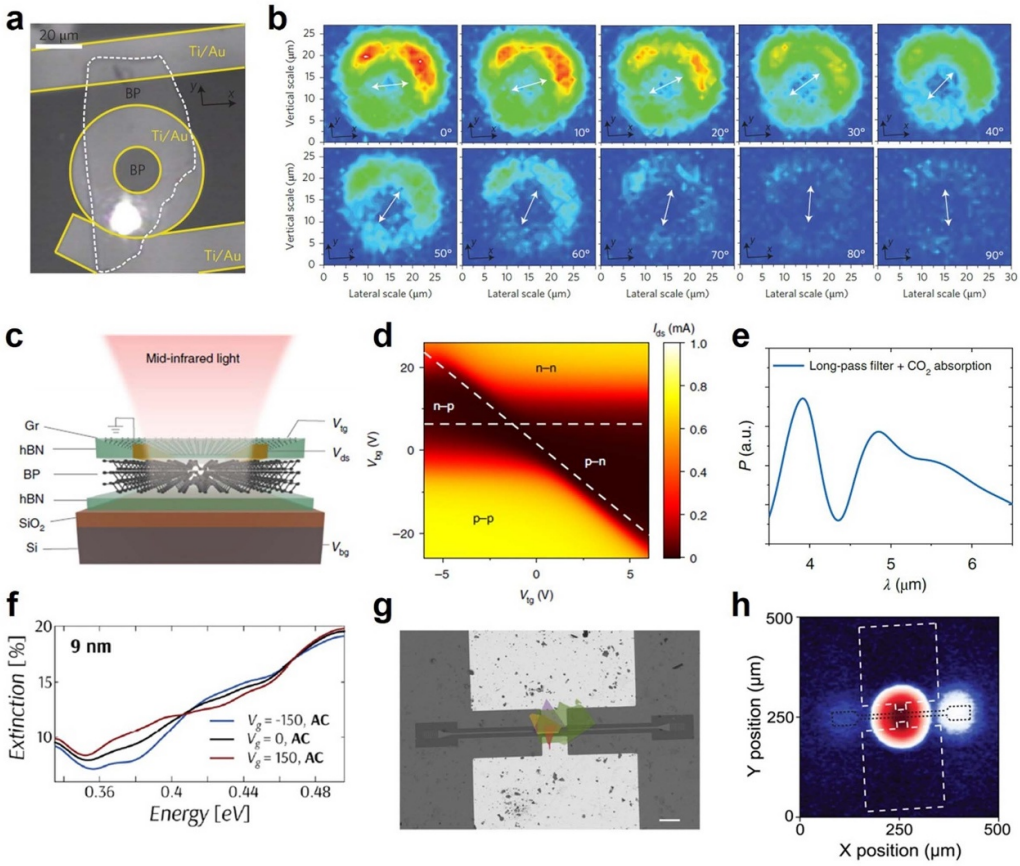

Figure 10. Interface and surface engineering of BP for optoelectronic applications. (a), (b) BP vertical p–n junction-based photodetector with polarization sensitivity. Reprinted from [30] by permission from Springer Nature Customer Service Centre GmbH. (a) Optical microscope image of the device that a ring-shaped Ti/Au electrode is applied to avoid the extra polarization originating from the straight edge of the metal. (b) Photocurrent mapping images of the BP inside the ring electrode under a linear-polarized light with the polarization direction from 0° to 90°. (c)–(e) A concept of proof of a BP-based MIR spectrometer. Reprinted from [162] by permission from Springer Nature Customer Service Centre GmbH. (c) Schematic illustration of the hBN/BP/hBN heterostructure-based spectrometer. (d) An array of source-drain current with different values of the top-gate (V_{tg}) and back-gate (V_{bg}) voltages. (e) The optical absorption spectrum of CO_2 which is captured and reconstructed by the BP spectrometer. (f) Optical extinction spectra of a BP-based electro-optical modulator, indicating an up to 6% modulation depth with the gate bias from −150 to 150 V. Reprinted with permission from [163], copyright (2017) American Chemical Society. (g), (h) Waveguide-integrated MIR LEDs based on the BP functional layer. Reprinted with permission from [46], copyright (2020) American Chemical Society. (g) SEM image of BP LED integrated on a waveguide. The stacked van der Waals layers including BP functional layer, two graphite electrodes, and an hBN encapsulation layer. (h) The spatially resolved electroluminescence mapping image of the LED, where the white dash lines draw two electrodes and the dark dash line draws the silicon waveguide.

(I_{ds}) mapping with top and bottom gate biases, in which four regions can be divided based on the polarities in the source-drain channel. By a learning process under 41 different displacements fields, spectral responsivity vectors are generated and a spectral responsivity matrix is constructed. As a demonstration, the single-detector-based spectrometer can successfully capture the optical absorption spectrum of carbon dioxide (CO_2) with moderate resolution (figure 10(e)).

Waveguide-based photodetectors have been very promising due to their compatibility with CMOS circuits and the ultrahigh integration [38, 155, 158, 160, 161]. By integrating 2D materials with low-loss waveguides, the BP-dielectric interface is formed and the optical interaction length of 2D materials is extended, which can enhance the optical absorption of 2D materials, so waveguide-based 2D photodetectors commonly have high responsivity and detectivity. In 2015, Si-waveguide integrated BP photodetector is firstly realized with a high photoresponsivity of ∼135 mA W^{-1}, a low dark current of 220 nA, and a fast response with a cut-off frequency up to 2.8 GHz [38]. Compared to the graphene photodetector with the same device structure, the dark current of BP photodetector is three orders of magnitude lower due to the open of the direct bandgap. Chen *et al* exploit the plasmonic structures into the waveguide integrated BP photodetector system [155]. The Au plasmonic nanostructure is aligned between the BP functional layer and the silicon dielectric waveguide to form a BP-metal interface, which achieves the low-loss of light propagation, confines the optical field below the diffraction limit, and drastically enhances the optical field of the light–BP interaction. The responsivity is highly at 10 A W^{-1} while the 3 dB cut-off frequency is ∼150 MHz. According to Huang *et al*, the work wavelength of waveguide integrated BP photodetectors is extended to MIR region [29]. The waveguide system contains an input grating and an output grating,

then 200 nm planarized SiO_2 is used as the insulation and passivation layer. BP with 23 nm thickness is transferred onto the SiO_2 layer. The Al_2O_3 layer with 20 nm thickness acts the dielectric for separating the channel and gate tuning. Due to the small bandgap of BP (∼0.3 eV), the cutoff wavelength of the device is 4.13 μm. The responsivity is 23 A W^{-1} and shows anisotropic characteristics. By adopting a silicon-on-insulator (SOI) ridge waveguide, Yin *et al* presents a hybrid silicon/BP waveguide photodetector and achieves the high-speed response with the 3 dB cut-off frequency of 1.33 GHz at 2 μm [161]. The response speed is restricted by the RC-constant and can be further improved by reducing the BP capacitance and the BP-metal contact resistance.

5.2. Electro-optical modulators

Owing to the solid electro-optical response and relatively small bandgap, BP is an excellent midinfrared Electro-optic material for modulation applications [33, 133]. In 2016, Lin *et al* proposed a proof-of-concept of BP-assisted electro-absorption modulator, in which BP thin film is placed on the top of Silicon waveguide and encapsulated by a 7 nm Al_2O_3 spacer, where the BP-dielectric interface is engineered and the electro-optical effects are studied [33]. By choosing a suitable thickness of BP, the device can operate at 2.1–3.3 μm. According to the simulation results, the BP-assisted modulator has a large modulation level (0.05 dB μm^{-1}), a low work voltage (62% reduction compared to graphene-based device), and a high ON-OFF ratio of extinction (exceeding the performance of SiGe modulators). Soon after, Peng *et al* experimentally demonstrated a BP-based MIR modulator by using the quantum confined Franz–Keldysh effect as the dominant mechanism [163]. The exfoliated multilayer BP is transferred on the SiO_2 substrate. The thickness of SiO_2 is set to be 450 nm for enhanced mid-IR absorption in BP. A 10 nm Al_2O_3 is deposited on BP as the encapsulated and protective layer. The optical absorption modulation is achieved up to 3% with the applied gate bias adjusting from 0 to 150 V (figure 10(f)). The performance of the device would be further improved if using high-k dielectric materials as the gate oxide. Besides, due to the anisotropic optical-electric effects, BP also has application potential to modulate light polarization and propagation direction [134].

5.3. Light emission diodes

Van der Waals based light-emission devices (LEDs) is attractive due to the high degree of confinement of 2D materials and the ease of integration with silicon chips. The heterojunction constructions of BP with other 2D semiconductors extend the operation wavelength of Van der Waals based LEDs to the MIR waveband [113, 164]. For example, Wang *et al* demonstrate a BP-MoS_2 based LED with the type-II heterojunction alignment, in which the polarized electroluminescence is emitted at 3.68 μm under room-temperature [164]. When applied a negative drain-source bias, the hot electrons in MoS_2 inject into the BP layer, which enhances the luminescence efficiency of BP. An on–off ratio highly at 10^5 and A room temperature internal quantum efficiencies of ∼1% have been achieved in the BP-based MIR LED. The anisotropic characteristics in BP-based LEDs have been observed that the electroluminescence (EL) intensity along the armchair axis is over seven times higher than that along the Zigzag axis [113].

Waveguide-integrated LEDs based on BP have also been realized, which are compatible with the silicon photonic platform [46]. The BP functional layer sandwiched by two graphite electrodes is transferred on a silicon waveguide fabricated on an SOI chip. By the encapsulation of hBN, an on-chip LED is constructed, where the emission light from BP can be evanescently coupled and then propagated through the silicon waveguide. The schematic diagram is in figure 10(g). The electroluminescence power at 3.6 μm is highly at 1.8 μW with excellent stability over 100 h, and the coupling efficiency is 10%. After further optimization, the measured emission intensity from the grating coupler would be more than 40% with respect to that from the BP emission region (figure 10(h)). Recently, using a dual-gating configuration, few-layer BP sandwiched by bottom and top hBN flakes can generate bright and wide-tunable PL from 3.7 to 7.7 μm, further indicating the potential of BP for the realization of future widely-tunable and polarized MIR LEDs [47].

5.4. All-optical modulators

All-optical modulators have been extensively utilized in ultrahigh bit rate communication systems due to the all-optical signal process with an ultrafast response and broad bandwidth. Furthermore, the all-optical modulation can be realized in simple configurations such as optical fibers or silicon waveguides, which have a miniature size for compact and integrated operation [165]. There are many different all-optical-modulators till now, including saturable absorbers [166–168], polarization controllers [169, 170], wavelength converters [171] and optical limiters [172]. The operation mechanisms of most of these devices are based on the strong optical nonlinearities of 2D materials (especially the third-order susceptibility). For example, the saturable absorption is originated from the imaginary part of the complex $\chi^{(3)}$ process, which is for passive mode-locking and Q-switching operations of lasers. In comparison, the real part of the complex $\chi^{(3)}$ process is responsible for Kerr effects, which can be employed for wavelength converters such as four-wave mixing (FWM) devices.

BP-based saturable absorbers are the earliest and most widely investigated photonic devices due to the growing need for ultrafast lasers. Till now, both mode-locking and Q-switching operations in NIR and MIR wavelengths have been achieved by BP-based saturable absorbers [48, 50, 173–176]. To realize a practical saturable absorption device, the instability of BP in the ambient environment is a problem. To avoid the oxidization of BP, Mu *et al* introduced a semi-industry approach of electrospinning to prepare robust BP-polymer networked membranes (figure 11(a)), in which BP nanosheets are uniformly distributed in PVP matrix [48]. The ultrafast and high-energy pulse generation is achieved in a 1550 nm

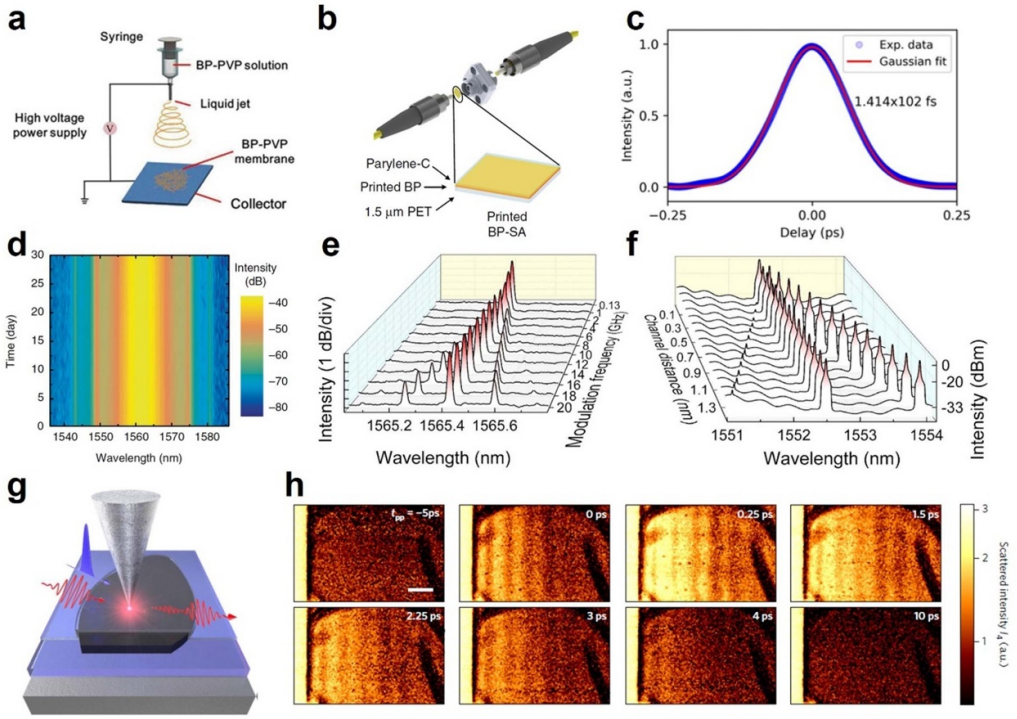

Figure 11. Interface and surface engineering of BP for photonic applications. (a) Electro-spun BP-PVP membrane for ultrafast pulse generations. Reproduced with permission from [48], John Wiley & Sons. [© 2015 WILEY-VCH Verlag GmbH & Co. KGaA, Weinheim]. (b)–(d) Ink-printed BP as saturable absorbers for mode-locked fiber lasers. Reproduced from [50]. CC BY 4.0. (b) Schematic illustration that shows two fiber end-facets sandwich the ink-printed BP membrane for fiber integration. (c) Autocorrelation trace of the obtained mode-locking pulses. (d) Wavelength spectra of long-term stable operation across 30 d. (e), (f) Four-wave mixing devices based on BP-deposited nonlinear fibers for all-optical modulation. Reproduced from [52]. CC BY 4.0. (e) Optical spectra of the generated signals by the four-wave mixing effects with the modulation frequency from 0.13 to 20 GHz. (f) Optical spectra of the signals evolving by tuning the channel distance from 0.1 to 1.3 nm. (g), (h) Ultrafast optical switch based on interface polaritons in the SiO_2/BP/SiO_2 heterostructure. Reprinted from [51] by permission from Springer Nature Customer Service Centre GmbH. (g) Schematic diagram of the setup and the device where two SiO_2 layers sandwich BP. (h) Scattered near-field intensity images in which the excitation and decay process of a hybrid phonon–plasmon–polariton mode are observed within a ten ps time scale.

fiber laser based on the optically transparent membrane with strong saturable absorption effects. Inkjet print is also a practical approach to achieve stable BP membranes [50, 176]. BP is dispersed in a binary solvent composed of isopropyl alcohol as a binder-free inkjet ink, allowing stable jetting with high printing consistency and spatial uniformity. As shown in figure 11(b), the as-printed BP membrane encapsulated by PET and perylene-C is integrated into the optical fiber system for mode-locking operations. The self-starting mode-locking with the pulse duration shortly at 102 fs is obtained in a dispersion-managed fiber laser cavity by the inkjet-printed BP, as shown in figure 11(c). When the laser continually operates over 30 days, the optical spectra still show no variations (figure 11(d)), indicating the long stability of inkjet-printed BP under ambient conditions.

BP wavelength converters have also been realized based on the large optical Kerr nonlinearity and the derivative FWM effects [52, 177]. BP is deposited on the D-shaped fiber to form BP-dielectric interface and interacts with the propagating light in the fiber through the evanescent field [52]. When two light beams with high power and different wavelength are incident into the nonlinear optical media BP, the FWM occurs and signals with new frequencies are converted. As shown in figure 11(e), the signal wavelength is fixed at 1552.6 nm, and the pump wavelength is tuned to 1559 nm, where a new signal at 1565.4 nm with two sub-bands is clearly observed. The modulation frequency is highly at 20 GHz, indicating that the ultrafast modulation is achieved by BP. When tuning the pump wavelength by 0.1 nm each time, the accordingly shift by 0.1 nm the generated signals is obtained in figure 11(f), which is the strong evidence of the FWM effects. However, due to the rapid degradation of BP under ambient conditions, the FWM-based wavelength converter lacks sufficient stability. Soon after, Zheng *et al* modified BP with metal-ion, in which the ambient stability is greatly enhanced [177]. Both the optical Kerr switching with an extinction ratio highly at 26 dB and the FWM operations with a conversion efficiency of −59.15 dB are experimentally realized by the BP-coated microfiber. By surface modifications, BP with a moderate direct bandgap and strong optical nonlinearity offers new opportunities to develop all-optical switches.

All-optical plasmonic modulators are new kinds of all-optical modulators with ultrahigh light confinement under the diffraction limit and ultra-low power consumption. The interface polaritons have realized the femtosecond photo-switching in SiO_2/BP/SiO_2 heterostructures [51]. The experimental

setup is in figure 11(g), in which a 1560 nm laser pumps the heterostructure with a pulse duration of ∼40 fs, and a MIR signal light is as the probe light. The photo-induced interband excitation is driven in BP but cannot be supported in SiO_2 due to its large-bandgap. The hybridization between the surface plasmon modes in BP and the surface phonon modes in SiO_2 is activated at around 38 THz by the interband excitation. The hybrid phonon–plasmon polariton mode is ultrafast switchable. As the recorded near-field snapshot images within 15 ps timescale in figure 11(h), the narrowband polaritons are launched with significant fringes. The response time of the amplitude saturation from zero to half its maximum is only ∼90 fs. The ultrafast switchable interface mode has a confined region and long propagation length, owing to the phonon-like nature within the Reststrahlen band [178]. BP-based heterostructures as a robust technological platform are promising for polariton-based mid-infrared photonics.

6. Conclusion and perspectives

In conclusion, we highlight and review the recent progress of interface and surface engineering strategies based on BP towards high-performance optoelectronics and photonics. Outstanding issues, including the construction of homo- and heterostructures with tailored band alignment, the reduction of Schottky barriers in metal-semiconductor contacts, and the achievement of giant quantum-confined Stark effects, have been made on different optoelectronic devices, such as photodetectors, spectrometers, electro-optical modulators, and LEDs. In addition, due to the solid dielectric screening, BP has strong exciton absorption with large binding energy. By introducing some strategies, including ultrafast exciton dissociation by constructing heterostructure, enhanced light-matter interactions by metal nanostructure, and surface modifications, BP is promising for photonic applications such as all-optical modulators and polariton devices.

Despite significant advances, BP-based applications are still in the early stages and have many challenges. Firstly, most current approaches, including surface passivation and encapsulation for achieving stable BP, are based on exfoliated BP samples, in which the flake size is minimal. Therefore, it is still very challenging to realize the high stability of large-scale BP and related devices in ambient conditions. In our opinion, the combination of chemical functional BP with a high functionalization degree and atomic layer deposition (ALD) physical passivation layers would be a promising approach for producing large-scale and large-area air-stabilized BP. Secondly, though different BP-based optoelectronic devices have been demonstrated with high performance, integrating LEDs, modulators, and photodetectors as a versatile system is still a problem. Finally, in spite of the fact that many-body interactions such as anisotropic interlayer exciton plasmon-phonon polaritons have been observed at the interface of BP, the novel polariton devices based on BP are still in concept, which needs to be developed in future BP-based photonics. Overall, as an ideal 2D platform with intriguing properties, BP is promising for future optoelectronics and photonics by a practical approach to interface and surface engineering.

Acknowledgment

This work was financially supported by the Starting Research Funds from Songshan Lake Materials Laboratory, China (No. Y0D1051F211).

ORCID iD

Shenghuang Lin https://orcid.org/0000-0001-9552-4680

References

[1] Bridgman P W 1914 Two new modifications of phosphorus *J. Am. Chem. Soc.* **36** 1344–63
[2] Geim A K and Novoselov K S 2007 The rise of graphene *Nat. Mater.* **6** 183–91
[3] Novoselov K S, Geim A K, Morozov S V, Jiang D, Zhang Y, Dubonos S V, Grigorieva I V and Firsov A A 2004 Electric field effect in atomically thin carbon films *Science* **306** 666–9
[4] Geim A K 2009 Graphene: status and prospects *Science* **324** 1530–4
[5] Xu M S, Liang T, Shi M M and Chen H Z 2013 Graphene-like two-dimensional materials *Chem. Rev.* **113** 3766–98
[6] Mak K F, Lee C, Hone J, Shan J and Heinz T F 2010 Atomically thin MoS_2: a new direct-gap semiconductor *Phys. Rev. Lett.* **105** 136805
[7] Wang Q H, Kalantar-Zadeh K, Kis A, Coleman J N and Strano M S 2012 Electronics and optoelectronics of two-dimensional transition metal dichalcogenides *Nat. Nanotechnol.* **7** 699–712
[8] Butler S Z *et al* 2013 Progress, challenges, and opportunities in two-dimensional materials beyond graphene *ACS Nano* **7** 2898–926
[9] Novoselov K S, Mishchenko A, Carvalho A and Neto A H C 2016 2D materials and van der Waals heterostructures *Science* **353** 9439
[10] Li L, Yu Y, Ye G J, Ge Q, Ou X, Wu H, Feng D, Chen X H and Zhang Y 2014 Black phosphorus field-effect transistors *Nat. Nanotechnol.* **9** 372–7
[11] Gusmao R, Sofer Z and Pumera M 2017 Black phosphorus rediscovered: from bulk material to monolayers *Angew. Chem., Int. Ed.* **56** 8052–72
[12] Deng B C, Frisenda R, Li C, Chen X L, Castellanos-Gomez A and Xia F N 2018 Progress on black phosphorus photonics *Adv. Opt. Mater.* **6** 1800365
[13] Han R Y, Feng S, Sun D M and Cheng H M 2021 Properties and photodetector applications of two-dimensional black arsenic phosphorus and black phosphorus *Sci. China Inf. Sci.* **64** 140402
[14] Liu H, Neal A T, Zhu Z, Luo Z, Xu X, Tománek D and Ye P D 2014 Phosphorene: an unexplored 2D semiconductor with a high hole mobility *ACS Nano* **8** 4033–41
[15] Xia F, Wang H and Jia Y 2014 Rediscovering black phosphorus as an anisotropic layered material for optoelectronics and electronics *Nat. Commun.* **5** 1–6
[16] Qiao J, Kong X, Hu Z-X, Yang F and Ji W 2014 High-mobility transport anisotropy and linear dichroism in few-layer black phosphorus *Nat. Commun.* **5** 1–7

[17] Chen C, Chen F, Chen X, Deng B, Eng B, Jung D, Guo Q, Yuan S, Watanabe K and Taniguchi T 2019 Bright mid-infrared photoluminescence from thin-film black phosphorus *Nano Lett.* **19** 1488–93

[18] Low T, Rodin A, Carvalho A, Jiang Y, Wang H, Xia F and Neto A C 2014 Tunable optical properties of multilayer black phosphorus thin films *Phys. Rev.* B **90** 075434

[19] Kim J, Baik S S, Ryu S H, Sohn Y, Park S, Park B-G, Denlinger J, Yi Y, Choi H J and Kim K S 2015 Observation of tunable band gap and anisotropic Dirac semimetal state in black phosphorus *Science* **349** 723–6

[20] Li L, Kim J, Jin C, Ye G J, Qiu D Y, Felipe H, Shi Z, Chen L, Zhang Z and Yang F 2017 Direct observation of the layer-dependent electronic structure in phosphorene *Nat. Nanotechnol.* **12** 21–25

[21] Tran V, Soklaski R, Liang Y and Yang L 2014 Layer-controlled band gap and anisotropic excitons in few-layer black phosphorus *Phys. Rev.* B **89** 235319

[22] Wang X, Jones A M, Seyler K L, Tran V, Jia Y, Zhao H, Wang H, Yang L, Xu X and Xia F 2015 Highly anisotropic and robust excitons in monolayer black phosphorus *Nat. Nanotechnol.* **10** 517–21

[23] Zhang G, Chaves A, Huang S, Wang F, Xing Q, Low T and Yan H 2018 Determination of layer-dependent exciton binding energies in few-layer black phosphorus *Sci. Adv.* **4** eaap9977

[24] Xu R, Yang J, Myint Y W, Pei J, Yan H, Wang F and Lu Y 2016 Exciton brightening in monolayer phosphorene via dimensionality modification *Adv. Mater.* **28** 3493–8

[25] Rudenko A, Yuan S and Katsnelson M 2015 Toward a realistic description of multilayer black phosphorus: from *GW* approximation to large-scale tight-binding simulations *Phys. Rev.* B **92** 085419

[26] Buscema M, Groenendijk D J, Blanter S I, Steele G A, van der Zant H S J and Castellanos-Gomez A 2014 Fast and broadband photoresponse of few-layer black phosphorus field-effect transistors *Nano Lett.* **14** 3347–52

[27] Wood J D, Wells S A, Jariwala D, Chen K S, Cho E, Sangwan V K, Liu X L, Lauhon L J, Marks T J and Hersam M C 2014 Effective passivation of exfoliated black phosphorus transistors against ambient degradation *Nano Lett.* **14** 6964–70

[28] Ling X, Wang H, Huang S X, Xia F N and Dresselhaus M S 2015 The renaissance of black phosphorus *Proc. Natl Acad. Sci.* **112** 4523–30

[29] Huang M, Li S, Zhang Z, Xiong X, Li X and Wu Y 2017 Multifunctional high-performance van der Waals heterostructures *Nat. Nanotechnol.* **12** 1148–54

[30] Yuan H T *et al* 2015 Polarization-sensitive broadband photodetector using a black phosphorus vertical p–n junction *Nat. Nanotechnol.* **10** 707–13

[31] Viti L, Hu J, Coquillat D, Knap W, Tredicucci A, Politano A and Vitiello M S 2015 Black phosphorus terahertz photodetectors *Adv. Mater.* **27** 5567–72

[32] Guo Q S *et al* 2016 Black phosphorus mid-infrared photodetectors with high gain *Nano Lett.* **16** 4648–55

[33] Lin C, Grassi R, Low T and Helmy A S 2016 Multilayer black phosphorus as a versatile mid-infrared electro-optic material *Nano Lett.* **16** 1683–9

[34] Mao N, Tang J, Xie L, Wu J, Han B, Lin J, Deng S, Ji W, Xu H and Liu K 2016 Optical anisotropy of black phosphorus in the visible regime *J. Am. Chem. Soc.* **138** 300–5

[35] Jiang H, Shi H, Sun X and Gao B 2018 Optical anisotropy of few-layer black phosphorus visualized by scanning polarization modulation microscopy *ACS Photonics* **5** 2509–15

[36] Li J 2020 Anisotropic interlayer exciton in black phosphorus van der Waals heterostructures *Opt. Quant. Electron.* **52** 1–9

[37] Engel M, Steiner M and Avouris P 2014 Black phosphorus photodetector for multispectral, high-resolution imaging *Nano Lett.* **14** 6414–7

[38] Youngblood N, Chen C, Koester S J and Li M 2015 Waveguide-integrated black phosphorus photodetector with high responsivity and low dark current *Nat. Photon.* **9** 247–52

[39] Huang M Q, Wang M L, Chen C, Ma Z W, Li X F, Han J B and Wu Y Q 2016 Broadband black-phosphorus photodetectors with high responsivity *Adv. Mater.* **28** 3481–5

[40] Buscema M, Groenendijk D J, Steele G A, Van Der Zant H S and Castellanos-Gomez A 2014 Photovoltaic effect in few-layer black phosphorus PN junctions defined by local electrostatic gating *Nat. Commun.* **5** 1–6

[41] Dai J and Zeng X C 2014 Bilayer phosphorene: effect of stacking order on bandgap and its potential applications in thin-film solar cells *J. Phys. Chem. Lett.* **5** 1289–93

[42] Liu Y D, Cai Y Q, Zhang G, Zhang Y W and Ang K W 2017 Al-doped black phosphorus p–n homojunction diode for high performance photovoltaic *Adv. Funct. Mater.* **27** 1604638

[43] Lin S H *et al* 2016 Solution-processable ultrathin black phosphorus as an effective electron transport layer in organic photovoltaics *Adv. Funct. Mater.* **26** 864–71

[44] Fu N Q *et al* 2018 Black phosphorus quantum dots as dual-functional electron-selective materials for efficient plastic perovskite solar cells *J. Mater. Chem.* A **6** 8886–94

[45] Zhang S, Yang J, Xu R, Wang F, Li W, Ghufran M, Zhang Y-W, Yu Z, Zhang G and Qin Q 2014 Extraordinary photoluminescence and strong temperature/angle-dependent Raman responses in few-layer phosphorene *ACS Nano* **8** 9590–6

[46] Chang T-Y, Chen Y, Luo D-I, Li J-X, Chen P-L, Lee S, Fang Z, Li W-Q, Zhang Y-Y and Li M 2020 Black phosphorus mid-infrared light-emitting diodes integrated with silicon photonic waveguides *Nano Lett.* **20** 6824–30

[47] Chen C, Lu X, Deng B, Chen X, Guo Q, Li C, Ma C, Yuan S, Sung E and Watanabe K 2020 Widely tunable mid-infrared light emission in thin-film black phosphorus *Sci. Adv.* **6** eaay6134

[48] Mu H, Lin S, Wang Z, Xiao S, Li P, Chen Y, Zhang H, Bao H, Lau S P and Pan C 2015 Black phosphorus–polymer composites for pulsed lasers *Adv. Opt. Mater.* **3** 1447–53

[49] Sotor J, Sobon G, Macherzynski W, Paletko P and Abramski K M 2015 Black phosphorus saturable absorber for ultrashort pulse generation *Appl. Phys. Lett.* **107** 051108

[50] Hu G, Albrow-Owen T, Jin X, Ali A, Hu Y, Howe R C, Shehzad K, Yang Z, Zhu X and Woodward R I 2017 Black phosphorus ink formulation for inkjet printing of optoelectronics and photonics *Nat. Commun.* **8** 1–10

[51] Huber M A *et al* 2017 Femtosecond photo-switching of interface polaritons in black phosphorus heterostructures *Nat. Nanotechnol.* **12** 207

[52] Uddin S, Debnath P C, Park K and Song Y-W 2017 Nonlinear black phosphorus for ultrafast optical switching *Sci. Rep.* **7** 1–8

[53] Hong H, Liu C, Cao T, Jin C, Wang S, Wang F and Liu K 2017 Interfacial engineering of van der Waals coupled 2D layered materials *Adv. Mater. Interfaces* **4** 1601054

[54] Jiang B, Yang Z, Liu X, Liu Y and Liao L 2019 Interface engineering for two-dimensional semiconductor transistors *Nano Today* **25** 122–34

[55] Hu Z H, Wu Z T, Han C, He J, Ni Z H and Chen W 2018 Two-dimensional transition metal dichalcogenides:

interface and defect engineering *Chem. Soc. Rev.* **47** 3100–28
[56] Zhang J L, Han C, Hu Z H, Wang L, Liu L, Wee A T S and Chen W 2018 2D phosphorene: epitaxial growth and interface engineering for electronic devices *Adv. Mater.* **30** 1870359
[57] Liu Y, Chen M and Yang S 2021 Chemical functionalization of 2D black phosphorus *InfoMat* **3** 231–51
[58] Yu X C, Zhang S L, Zeng H B and Wang Q J 2016 Lateral black phosphorene P–N junctions formed via chemical doping for high performance near-infrared photodetector *Nano Energy* **25** 34–41
[59] Nie Z, Wang Y, Li Z, Sun Y, Qin S, Liu X, Turcu I, Shi Y, Zhang R and Ye Y 2019 Ultrafast free carrier dynamics in black phosphorus–molybdenum disulfide (BP/MoS 2) heterostructures *Nanoscale Horiz.* **4** 1099–105
[60] Qiu D Y, Da Jornada F H and Louie S G 2017 Environmental screening effects in 2D materials: renormalization of the bandgap, electronic structure, and optical spectra of few-layer black phosphorus *Nano Lett.* **17** 4706–12
[61] Yuan J, Najmaei S, Zhang Z, Zhang J, Lei S, Ajayan P M, Yakobson B I and Lou J 2015 Photoluminescence quenching and charge transfer in artificial heterostacks of monolayer transition metal dichalcogenides and few-layer black phosphorus *ACS Nano* **9** 555–63
[62] Yuan L, Zheng B, Kunstmann J, Brumme T, Kuc A B, Ma C, Deng S, Blach D, Pan A and Huang L 2020 Twist-angle-dependent interlayer exciton diffusion in WS_2–WSe_2 heterobilayers *Nat. Mater.* **19** 617–23
[63] Liu C, Xiong C, Li M, Ruan B, Zhang B, Wu K, Chang X, Xie W and Li H 2021 Rabi splitting obtained in exciton-plasmon polaritons coupling between monolayer black phosphorus with metal *Appl. Phys. Express* **14** 086001
[64] Ryder C R, Wood J D, Wells S A, Yang Y, Jariwala D, Marks T J, Schatz G C and Hersam M C 2016 Covalent functionalization and passivation of exfoliated black phosphorus via aryl diazonium chemistry *Nat. Chem.* **8** 597–602
[65] Zhao Y, Wang H, Huang H, Xiao Q, Xu Y, Guo Z, Xie H, Shao J, Sun Z and Han W 2016 Surface coordination of black phosphorus for robust air and water stability *Angew. Chem., Int. Ed.* **128** 5087–91
[66] Wild S, Dinh X T, Maid H, Hauke F, Abellán G and Hirsch A 2020 Quantifying the covalent functionalization of black phosphorus *Angew. Chem., Int. Ed.* **59** 20230–4
[67] Li X-B, Guo P, Cao T-F, Liu H, Lau W-M and Liu L-M 2015 Structures, stabilities and electronic properties of defects in monolayer black phosphorus *Sci. Rep.* **5** 1–11
[68] Rudenko A N and Katsnelson M I 2014 Quasiparticle band structure and tight-binding model for single-and bilayer black phosphorus *Phys. Rev.* B **89** 201408
[69] Keyes R W 1953 The electrical properties of black phosphorus *Phys. Rev.* **92** 580
[70] Warschauer D 1963 Electrical and optical properties of crystalline black phosphorus *J. Appl. Phys.* **34** 1853–60
[71] Guo Y and Robertson J 2015 Vacancy and doping states in monolayer and bulk black phosphorus *Sci. Rep.* **5** 1–10
[72] Ugeda M M, Bradley A J, Shi S-F, Felipe H, Zhang Y, Qiu D Y, Ruan W, Mo S-K, Hussain Z and Shen Z-X 2014 Giant bandgap renormalization and excitonic effects in a monolayer transition metal dichalcogenide semiconductor *Nat. Mater.* **13** 1091–5
[73] Fang H, Bechtel H A, Plis E, Martin M C, Krishna S, Yablonovitch E and Javey A 2013 Quantum of optical absorption in two-dimensional semiconductors *Proc. Natl Acad. Sci.* **110** 11688–91
[74] Yang J, Xu R, Pei J, Myint Y W, Wang F, Wang Z, Zhang S, Yu Z and Lu Y 2015 Optical tuning of exciton and trion emissions in monolayer phosphorene *Light Sci. Appl.* **4** e312
[75] Xu R, Zhang S, Wang F, Yang J, Wang Z, Pei J, Myint Y W, Xing B, Yu Z and Fu L 2016 Extraordinarily bound quasi-one-dimensional trions in two-dimensional phosphorene atomic semiconductors *ACS Nano* **10** 2046–53
[76] Rodin A, Carvalho A and Neto A C 2014 Excitons in anisotropic two-dimensional semiconducting crystals *Phys. Rev.* B **90** 075429
[77] Zhang G, Huang S, Chaves A, Song C, Özçelik V O, Low T and Yan H 2017 Infrared fingerprints of few-layer black phosphorus *Nat. Commun.* **8** 1
[78] Low T, Roldán R, Wang H, Xia F, Avouris P, Moreno L M and Guinea F 2014 Plasmons and screening in monolayer and multilayer black phosphorus *Phys. Rev. Lett.* **113** 106802
[79] Arra S, Babar R and Kabir M 2019 Exciton in phosphorene: strain, impurity, thickness, and heterostructure *Phys. Rev.* B **99** 045432
[80] Nemilentsau A, Low T and Hanson G 2016 Anisotropic 2D materials for tunable hyperbolic plasmonics *Phys. Rev. Lett.* **116** 066804
[81] Correas-Serrano D, Gomez-Diaz J, Melcon A A and Alù A 2016 Black phosphorus plasmonics: anisotropic elliptical propagation and nonlocality-induced canalization *J. Opt.* **18** 104006
[82] Yin X, Ye Z, Chenet D A, Ye Y, O'Brien K, Hone J C and Zhang X 2014 Edge nonlinear optics on a MoS_2 atomic monolayer *Science* **344** 488–90
[83] Malard L M, Alencar T V, Barboza A P M, Mak K F and De Paula A M 2013 Observation of intense second harmonic generation from MoS_2 atomic crystals *Phys. Rev.* B **87** 201401
[84] Wang G, Marie X, Gerber I, Amand T, Lagarde D, Bouet L, Vidal M, Balocchi A and Urbaszek B 2015 Giant enhancement of the optical second-harmonic emission of WSe_2 monolayers by laser excitation at exciton resonances *Phys. Rev. Lett.* **114** 097403
[85] Seyler K L, Schaibley J R, Gong P, Rivera P, Jones A M, Wu S, Yan J, Mandrus D G, Yao W and Xu X 2015 Electrical control of second-harmonic generation in a WSe_2 monolayer transistor *Nat. Nanotechnol.* **10** 407–11
[86] Li Y, Rao Y, Mak K F, You Y, Wang S, Dean C R and Heinz T F 2013 Probing symmetry properties of few-layer MoS_2 and h-BN by optical second-harmonic generation *Nano Lett.* **13** 3329–33
[87] Christensen T, Yan W, Jauho A-P, Wubs M and Mortensen N A 2015 Kerr nonlinearity and plasmonic bistability in graphene nanoribbons *Phys. Rev.* B **92** 121407
[88] Vermeulen N, Castelló-Lurbe D, Cheng J, Pasternak I, Krajewska A, Ciuk T, Strupinski W, Thienpont H and Van Erps J 2016 Negative Kerr nonlinearity of graphene as seen via chirped-pulse-pumped self-phase modulation *Phys. Rev. Appl.* **6** 044006
[89] Youngblood N, Peng R, Nemilentsau A, Low T and Li M 2017 Layer-tunable third-harmonic generation in multilayer black phosphorus *ACS Photonics* **4** 8–14
[90] Karvonen L, Säynätjoki A, Mehravar S, Rodriguez R D, Hartmann S, Zahn D R, Honkanen S, Norwood R A, Peyghambarian N and Kieu K 2015 Investigation of second-and third-harmonic generation in few-layer gallium selenide by multiphoton microscopy *Sci. Rep.* **5** 1–8
[91] Lu S, Miao L, Guo Z, Qi X, Zhao C, Zhang H, Wen S, Tang D and Fan D 2015 Broadband nonlinear optical response in multi-layer black phosphorus: an emerging infrared and mid-infrared optical material *Opt. Express* **23** 11183–94

[92] Margulis V A, Muryumin E and Gaiduk E 2018 Optical Kerr effect and two-photon absorption in monolayer black phosphorus *J. Opt.* **20** 055503

[93] Wang K, Szydłowska B M, Wang G, Zhang X, Wang J J, Magan J J, Zhang L, Coleman J N, Wang J and Blau W J 2016 Ultrafast nonlinear excitation dynamics of black phosphorus nanosheets from visible to mid-infrared *ACS Nano* **10** 6923–32

[94] Zhang R, Zhang Y, Yu H, Zhang H, Yang R, Yang B, Liu Z and Wang J 2015 Broadband black phosphorus optical modulator in the spectral range from visible to mid-infrared *Adv. Opt. Mater.* **3** 1787–92

[95] Wang Y, Liu S, Zeng B, Huang H, Xiao J, Li J, Long M, Xiao S, Yu X and Gao Y 2017 Ultraviolet saturable absorption and ultrafast carrier dynamics in ultrasmall black phosphorus quantum dots *Nanoscale* **9** 4683–90

[96] Wang Y, Huang G, Mu H, Lin S, Chen J, Xiao S, Bao Q and He J 2015 Ultrafast recovery time and broadband saturable absorption properties of black phosphorus suspension *Appl. Phys. Lett.* **107** 091905

[97] Yau S-L, Moffat T P, Bard A J, Zhang Z and Lerner M M 1992 STM of the (010) surface of orthorhombic phosphorus *Chem. Phys. Lett.* **198** 383–8

[98] Brunner J, Thüler M, Veprek S and Wild R 1979 X-ray photoelectron study of amorphous phosphorus preparedbyplasmachemical transport. Comparison with crystalline polymorphs *J. Phys. Chem. Solids* **40** 967–71

[99] Island J O, Steele G A, van der Zant H S and Castellanos-Gomez A 2015 Environmental instability of few-layer black phosphorus *2D Mater.* **2** 011002

[100] Huang Y, Qiao J, He K, Bliznakov S, Sutter E, Chen X, Luo D, Meng F, Su D and Decker J 2016 Interaction of black phosphorus with oxygen and water *Chem. Mater.* **28** 8330–9

[101] Walia S, Sabri Y, Ahmed T, Field M R, Ramanathan R, Arash A, Bhargava S K, Sriram S, Bhaskaran M and Bansal V 2016 Defining the role of humidity in the ambient degradation of few-layer black phosphorus *2D Mater.* **4** 015025

[102] Zhou Q, Chen Q, Tong Y and Wang J 2016 Light-induced ambient degradation of few-layer black phosphorus: mechanism and protection *Angew. Chem., Int. Ed.* **55** 11437–41

[103] Han C, Hu Z, Carvalho A, Guo N, Zhang J, Hu F, Xiang D, Wu J, Lei B and Wang L 2017 Oxygen induced strong mobility modulation in few-layer black phosphorus *2D Mater.* **4** 021007

[104] Favron A, Gaufrès E, Fossard F, Phaneuf-L'Heureux A-L, Tang N Y, Lévesque P L, Loiseau A, Leonelli R, Francoeur S and Martel R 2015 Photooxidation and quantum confinement effects in exfoliated black phosphorus *Nat. Mater.* **14** 826–32

[105] Wang F, Zhang G, Huang S, Song C, Wang C, Xing Q, Lei Y and Yan H 2019 Electronic structures of air-exposed few-layer black phosphorus by optical spectroscopy *Phys. Rev.* B **99** 075427

[106] Wang F K, Pei K, Li Y, Li H Q and Zhai T Y 2021 2D homojunctions for electronics and optoelectronics *Adv. Mater.* **33** 2005303

[107] Cao T, Li Z L, Qiu D Y and Louie S G 2016 Gate switchable transport and optical anisotropy in 90 degrees twisted bilayer black phosphorus *Nano Lett.* **16** 5542–6

[108] Liu N S, Zhang J F, Zhou S and Zhao J J 2020 Tuning the electronic properties of bilayer black phosphorene with the twist angle *J. Mater. Chem.* C **8** 6264–72

[109] Srivastava P K, Hassan Y, de Sousa D J, Gebredingle Y, Joe M, Ali F, Zheng Y, Yoo W J, Ghosh S and Teherani J T 2021 Resonant tunnelling diodes based on twisted black phosphorus homostructures *Nat. Electron* **4** 269–76

[110] Deng Y, Luo Z, Conrad N J, Liu H, Gong Y, Najmaei S, Ajayan P M, Lou J, Xu X and Ye P D 2014 Black phosphorus–monolayer MoS_2 van der Waals heterojunction p–n diode *ACS Nano* **8** 8292–9

[111] Liu B, Long M, Cai M-Q and Yang J 2018 Interface engineering of $CsPbI_3$-black phosphorus van der Waals heterostructure *Appl. Phys. Lett.* **112** 043901

[112] Cao Y, Mishchenko A, Yu G, Khestanova E, Rooney A, Prestat E, Kretinin A, Blake P, Shalom M B and Woods C 2015 Quality heterostructures from two-dimensional crystals unstable in air by their assembly in inert atmosphere *Nano Lett.* **15** 4914–21

[113] Zong X R *et al* 2020 Black phosphorus-based van der Waals heterostructures for mid-infrared light-emission applications *Light Sci. Appl.* **9** 114

[114] Srivastava P K, Hassan Y, Gebredingle Y, Jung J, Kang B, Yoo W J, Singh B and Lee C 2019 Van der Waals broken-gap p–n heterojunction tunnel diode based on black phosphorus and rhenium disulfide *ACS Appl. Mater. Interfaces* **11** 8266–75

[115] Shao W, Wang L, Wang H, Zhao Z, Zhang X, Jiang S, Chen S, Sun X, Zhang Q and Xie Y 2019 Efficient exciton dissociation in heterojunction interfaces realizing enhanced photoresponsive performance *J. Phys. Chem. Lett.* **10** 2904–10

[116] Zhou Q, Zhou H, Tao W, Zheng Y, Chen Y and Zhu H 2020 Highly efficient multiple exciton generation and harvesting in few-layer black phosphorus and heterostructure *Nano Lett.* **20** 8212–9

[117] Bayer M, Timofeev V, Faller F, Gutbrod T and Forchel A 1996 Direct and indirect excitons in coupled $GaAs/Al_{0.30}Ga_{0.70}As$ double quantum wells separated by AlAs barriers *Phys. Rev.* B **54** 8799

[118] Rivera P, Schaibley J R, Jones A M, Ross J S, Wu S, Aivazian G, Klement P, Seyler K, Clark G and Ghimire N J 2015 Observation of long-lived interlayer excitons in monolayer $MoSe_2$–WSe_2 heterostructures *Nat. Commun.* **6** 1–6

[119] Liu X, Watanabe K, Taniguchi T, Halperin B I and Kim P 2017 Quantum Hall drag of exciton condensate in graphene *Nat. Phys.* **13** 746–50

[120] Kogar A, Rak M S, Vig S, Husain A A, Flicker F, Joe Y I, Venema L, MacDougall G J, Chiang T C and Fradkin E 2017 Signatures of exciton condensation in a transition metal dichalcogenide *Science* **358** 1314–7

[121] Chen Y and Quek S Y 2018 Tunable bright interlayer excitons in few-layer black phosphorus based van der Waals heterostructures *2D Mater.* **5** 045031

[122] Du Y, Liu H, Deng Y and Ye P D 2014 Device perspective for black phosphorus field-effect transistors: contact resistance, ambipolar behavior, and scaling *ACS Nano* **8** 10035–42

[123] Liu H, Neal A T and Ye P D D 2012 Channel length scaling of MoS_2 MOSFETs *ACS Nano* **6** 8563–9

[124] Das S, Chen H Y, Penumatcha A V and Appenzeller J 2013 High performance multilayer MoS_2 transistors with scandium contacts *Nano Lett.* **13** 100–5

[125] Shen P-C, Su C, Lin Y, Chou A-S, Cheng C-C, Park J-H, Chiu M-H, Lu A-Y, Tang H-L and Tavakoli M M 2021 Ultralow contact resistance between semimetal and monolayer semiconductors *Nature* **593** 211–7

[126] Azar N S, Bullock J, Balendhran S, Kim H, Javey A and Crozier K B 2021 Light–matter interaction enhancement in anisotropic 2D black phosphorus via polarization-tailoring nano-optics *ACS Photonics* **8** 1120–8

[127] Kockum A F, Miranowicz A, De Liberato S, Savasta S and Nori F 2019 Ultrastrong coupling between light and matter *Nat. Rev. Phys.* **1** 19–40

[128] Dai X, Song C, Qiu C, Wu L and Xiang Y 2019 Theoretical investigation of multilayer $Ti_3C_2T_x$ MXene as the plasmonic material for surface plasmon resonance sensors in near infrared region *IEEE Sens. J.* **19** 11834–8

[129] Li M, Li H, Xu H, Xiong C, Zhao M, Liu C, Ruan B, Zhang B and Wu K 2020 Dual-frequency on–off modulation and slow light analysis based on dual plasmon-induced transparency in terahertz patterned graphene metamaterial *New J. Phys.* **22** 103030

[130] Kuo Y-H, Lee Y K, Ge Y, Ren S, Roth J E, Kamins T I, Miller D A and Harris J S 2005 Strong quantum-confined Stark effect in germanium quantum-well structures on silicon *Nature* **437** 1334–6

[131] Liu J, Beals M, Pomerene A, Bernardis S, Sun R, Cheng J, Kimerling L C and Michel J 2008 Waveguide-integrated, ultralow-energy GeSi electro-absorption modulators *Nat. Photon.* **2** 433–7

[132] Miller D A, Chemla D, Damen T, Gossard A, Wiegmann W, Wood T and Burrus C 1984 Band-edge electroabsorption in quantum well structures: the quantum-confined Stark effect *Phys. Rev. Lett.* **53** 2173

[133] Liu Y, Qiu Z, Carvalho A, Bao Y, Xu H, Tan S J, Liu W, Castro Neto A, Loh K P and Lu J 2017 Gate-tunable giant stark effect in few-layer black phosphorus *Nano Lett.* **17** 1970–7

[134] Sherrott M C, Whitney W S, Jariwala D, Biswas S, Went C M, Wong J, Rossman G R and Atwater H A 2018 Anisotropic quantum well electro-optics in few-layer black phosphorus *Nano Lett.* **19** 269–76

[135] Li L, Yang F, Ye G J, Zhang Z, Zhu Z, Lou W, Zhou X, Li L, Watanabe K and Taniguchi T 2016 Quantum Hall effect in black phosphorus two-dimensional electron system *Nat. Nanotechnol.* **11** 593–7

[136] Xiang D *et al* 2015 Surface transfer doping induced effective modulation on ambipolar characteristics of few-layer black phosphorus *Nat. Commun.* **6** 6485

[137] Deng B, Tran V, Xie Y, Jiang H, Li C, Guo Q, Wang X, Tian H, Koester S J and Wang H 2017 Efficient electrical control of thin-film black phosphorus bandgap *Nat. Commun.* **8** 1–7

[138] Koenig S P, Doganov R A, Seixas L, Carvalho A, Tan J Y, Watanabe K, Taniguchi T, Yakovlev N, Neto A H C and Ozyilmaz B 2016 Electron doping of ultrathin black phosphorus with Cu adatoms *Nano Lett.* **16** 2145–51

[139] Han C, Hu Z, Gomes L C, Bao Y, Carvalho A, Tan S J, Lei B, Xiang D, Wu J and Qi D 2017 Surface functionalization of black phosphorus via potassium toward high-performance complementary devices *Nano Lett.* **17** 4122–9

[140] Zheng Y, Hu Z, Han C, Guo R, Xiang D, Lei B, Wang Y, He J, Lai M and Chen W 2019 Black phosphorus inverter devices enabled by *in-situ* aluminum surface modification *Nano Res.* **12** 531–6

[141] Lee S W, Qiu L, Yoon J C, Kim Y, Li D, Oh I, Lee G-H, Yoo J-W, Shin H-J and Ding F 2021 Anisotropic angstrom-wide conductive channels in black phosphorus by top-down Cu intercalation *Nano Lett.* **21** 6336–42

[142] Wang Y, Zheng Y, Han C and Chen W 2021 Surface charge transfer doping for two-dimensional semiconductor-based electronic and optoelectronic devices *Nano Res.* **14** 1682–97

[143] Cai Y, Ke Q, Zhang G and Zhang Y-W 2015 Energetics, charge transfer, and magnetism of small molecules physisorbed on phosphorene *J. Phys. Chem.* C **119** 3102–10

[144] Artel V, Guo Q, Cohen H, Gasper R, Ramasubramaniam A, Xia F and Naveh D 2017 Protective molecular passivation of black phosphorus *npj 2D Mater. Appl.* **1** 1–5

[145] Kang D-H, Jeon M H, Jang S K, Choi W-Y, Kim K N, Kim J, Lee S, Yeom G Y and Park J-H 2017 Self-assembled layer (SAL)-based doping on black phosphorus (BP) transistor and photodetector *ACS Photonics* **4** 1822–30

[146] Pei J, Gai X, Yang J, Wang X, Yu Z, Choi D-Y, Luther-Davies B and Lu Y 2016 Producing air-stable monolayers of phosphorene and their defect engineering *Nat. Commun.* **7** 1–8

[147] Illarionov Y Y, Waltl M, Rzepa G, Kim J-S, Kim S, Dodabalapur A, Akinwande D and Grasser T 2016 Long-term stability and reliability of black phosphorus field-effect transistors *ACS Nano* **10** 9543–9

[148] Alsaffar F, Alodan S, Alrasheed A, Alhussain A, Alrubaiq N, Abbas A and Amer M R 2017 Raman sensitive degradation and etching dynamics of exfoliated black phosphorus *Sci. Rep.* **7** 1–9

[149] Zhao Y, Zhou Q, Li Q, Yao X and Wang J 2017 Passivation of black phosphorus via self-assembled organic monolayers by van der Waals epitaxy *Adv. Mater.* **29** 1603990

[150] Chen X, Wu Y, Wu Z, Han Y, Xu S, Wang L, Ye W, Han T, He Y and Cai Y 2015 High-quality sandwiched black phosphorus heterostructure and its quantum oscillations *Nat. Commun.* **6** 1–6

[151] Abellán G, Lloret V, Mundloch U, Marcia M, Neiss C, Görling A, Varela M, Hauke F and Hirsch A 2016 Noncovalent functionalization of black phosphorus *Angew. Chem.* **128** 14777–82

[152] Abellan G, Wild S, Lloret V, Scheuschner N, Gillen R, Mundloch U, Maultzsch J, Varela M, Hauke F and Hirsch A 2017 Fundamental insights into the degradation and stabilization of thin layer black phosphorus *J. Am. Chem. Soc.* **139** 10432–40

[153] Li D, Yu Y and Ning C-Z 2021 Super-stable high-quality few-layer black phosphorus for photonic applications *ACS Appl. Nano Mater.* **4** 4746–53

[154] Ye L, Li H, Chen Z and Xu J 2016 Near-infrared photodetector based on MoS_2/black phosphorus heterojunction *ACS Photonics* **3** 692–9

[155] Chen X, Lu X, Deng B, Sinai O, Shao Y, Li C, Yuan S, Tran V, Watanabe K and Taniguchi T 2017 Widely tunable black phosphorus mid-infrared photodetector *Nat. Commun.* **8** 1–7

[156] Zhu W, Xu H, Pan J, Zhang S, Zheng H, Zhong Y, Yu J and Chen Z 2020 Black phosphorus terahertz sensing based on photonic spin Hall effect *Opt. Express* **28** 25869–78

[157] Hong T, Chamlagain B, Lin W, Chuang H-J, Pan M, Zhou Z and Xu Y-Q 2014 Polarized photocurrent response in black phosphorus field-effect transistors *Nanoscale* **6** 8978–83

[158] Chen C, Youngblood N, Peng R, Yoo D, Mohr D A, Johnson T W, Oh S-H and Li M 2017 Three-dimensional integration of black phosphorus photodetector with silicon photonics and nanoplasmonics *Nano Lett.* **17** 985–91

[159] Bullock J, Amani M, Cho J, Chen Y-Z, Ahn G H, Adinolfi V, Shrestha V R, Gao Y, Crozier K B and Chueh Y-L 2018 Polarization-resolved black phosphorus/molybdenum disulfide mid-wave infrared photodiodes with high detectivity at room temperature *Nat. Photon.* **12** 601–7

[160] Huang L, Dong B, Guo X, Chang Y, Chen N, Huang X, Liao W, Zhu C, Wang H and Lee C 2018 Waveguide-integrated black phosphorus photodetector for mid-infrared applications *ACS Nano* **13** 913–21

[161] Yin Y, Cao R, Guo J, Liu C, Li J, Feng X, Wang H, Du W, Qadir A and Zhang H 2019 High-speed and high-responsivity hybrid silicon/black-phosphorus

waveguide photodetectors at 2 μm *Laser Photon. Rev.* **13** 1900032
[162] Yuan S, Naveh D, Watanabe K, Taniguchi T and Xia F 2021 A wavelength-scale black phosphorus spectrometer *Nat. Photon.* **15** 601–7
[163] Peng R, Khaliji K, Youngblood N, Grassi R, Low T and Li M 2017 Midinfrared electro-optic modulation in few-layer black phosphorus *Nano Lett.* **17** 6315–20
[164] Wang J, Rousseau A, Yang M, Low T, Francoeur S and Kéna-Cohen S 2020 Mid-infrared polarized emission from black phosphorus light-emitting diodes *Nano Lett.* **20** 3651–5
[165] Sun Z, Martinez A and Wang F 2016 Optical modulators with 2D layered materials *Nat. Photon.* **10** 227–38
[166] Bao Q, Zhang H, Wang Y, Ni Z, Yan Y, Shen Z X, Loh K P and Tang D Y 2009 Atomic-layer graphene as a saturable absorber for ultrafast pulsed lasers *Adv. Funct. Mater.* **19** 3077–83
[167] Mu H, Wang Z, Yuan J, Xiao S, Chen C, Chen Y, Chen Y, Song J, Wang Y and Xue Y 2015 Graphene–Bi_2Te_3 heterostructure as saturable absorber for short pulse generation *ACS Photonics* **2** 832–41
[168] Mu H, Liu Y, Bongu S R, Bao X, Li L, Xiao S, Zhuang J, Liu C, Huang Y and Dong Y 2021 Germanium nanosheets with dirac characteristics as a saturable absorber for ultrafast pulse generation *Adv. Mater.* **33** 2101042
[169] Wu J, Yang Y, Qu Y, Xu X, Liang Y, Chu S T, Little B E, Morandotti R, Jia B and Moss D J 2019 Graphene oxide waveguide and micro-ring resonator polarizers *Laser Photonics Rev.* **13** 1900056
[170] Bao Q, Zhang H, Wang B, Ni Z, Lim C H Y X, Wang Y, Tang D Y and Loh K P 2011 Broadband graphene polarizer *Nat. Photon.* **5** 411–5
[171] Hendry E, Hale P J, Moger J, Savchenko A and Mikhailov S A 2010 Coherent nonlinear optical response of graphene *Phys. Rev. Lett.* **105** 097401
[172] Wang J, Hernandez Y, Lotya M, Coleman J N and Blau W J 2009 Broadband nonlinear optical response of graphene dispersions *Adv. Mater.* **21** 2430–5
[173] Chen Y, Jiang G, Chen S, Guo Z, Yu X, Zhao C, Zhang H, Bao Q, Wen S and Tang D 2015 Mechanically exfoliated black phosphorus as a new saturable absorber for both Q-switching and mode-locking laser operation *Opt. Express* **23** 12823–33
[174] Pawliszewska M, Ge Y, Li Z, Zhang H and Sotor J 2017 Fundamental and harmonic mode-locking at 2.1 μm with black phosphorus saturable absorber *Opt. Express* **25** 16916–21
[175] Wang T, Zhang W, Shi X, Wang J, Ding X, Zhang K, Peng J, Wu J and Zhou P 2019 Black phosphorus-enabled harmonic mode locking of dark pulses in a Yb-doped fiber laser *Laser Phys. Lett.* **16** 085102
[176] Jin X, Hu G, Zhang M, Hu Y, Albrow-Owen T, Howe R C, Wu T-C, Wu Q, Zheng Z and Hasan T 2018 102 fs pulse generation from a long-term stable, inkjet-printed black phosphorus-mode-locked fiber laser *Opt. Express* **26** 12506–13
[177] Zheng J, Yang Z, Si C, Liang Z, Chen X, Cao R, Guo Z, Wang K, Zhang Y and Ji J 2017 Black phosphorus based all-optical-signal-processing: toward high performances and enhanced stability *ACS Photonics* **4** 1466–76
[178] Li P, Yang X, Maß T W, Hanss J, Lewin M, Michel A-K U, Wuttig M and Taubner T 2016 Reversible optical switching of highly confined phonon–polaritons with an ultrathin phase-change material *Nat. Mater.* **15** 870–5